Postprint of: Krzyżanowski J., Tejchman J., Sołowski W., Wójcik M., Modelling of shear zones during quasi-static granular silo flow using material point method (MPM), Powder Technology (2020), DOI: 10.1016/j.powtec.2020.10.001

Modelling of shear zones during quasi-static granular silo flow using material point method (MPM)

J. Krzyżanowski [a], J. Tejchman [a], W. Sołowski [b], M. Wójcik [a, *]

[a] *Gdańsk University of Technology, Narutowicza 11/12, 80-233, Gdańsk, Poland*
[b] *Aalto University, Finland*

A B S T R A C T

The paper focuses on confined silo flow of cohesionless sand. The problem considered is a quasi-static flow in a plane strain model silo with parallel walls simulated with the material point method (MPM). The simula-tion used a non-local hypoplastic constitutive model. Initially, the paper validated the implemented numerical approach with basic element tests and a plane strain compression test. The subsequent MPM calculations for a model silo were performed with different initial void ratios of sand and silo wall roughness. The flow simulations took also into account the different both location and width of the outlet. The emphasis was on the evolution of both shear zones (wall and internal curvilinear shear zones) and their impact on wall stresses/forces during flow. The numerical findings enhance the understanding of shear localization in granular mate-rials during confined controlled flow in silos and its immense effect on the magnitude and distribution of wall pressures.

Keywords:
MPM
Silo flow
Bulk solid
Shear zones
Wall pressure
Eccentric outlet

Article history:
Received 24 June 2020
Received in revised form 21 September 2020
Accepted 2 October 2020
Available online xxx

1. Introduction

Silos are engineering structures that are largely used in the industry for storing, feeding and processing bulk solids in agricultural, mining, mineral processing, chemical and shipping industries [1–4]. Although there exist extensive experimental and theoretical data on silo problems, the rate of silos failures is still much higher than the failures of other industrial structures [5–7]. Most of the silo failures happen during the emptying process of bulk solids which frequently leads to a collapse of entire structures. In general, these failures are due to weak knowledge of several complex characteristic phenomena that occur during bulk solid flow in the interaction with silo structures (e.g. shear localization, dynamic effects) [8–10]. Experiments in full-scale silos are obviously the best tool to investigate those phenomena. However, they are expensive, work-intensive and difficult to conduct (e.g. [11–13]). Therefore, numerical analyses are desired to reproduce experiments in silos for improving their design. The problem of granular silo flow is of high complexity. To realistically describe granular flow in silos within continuum mechanics to estimate wall pressures and determine flow patterns for the flowing material [8], some basic conditions should be fulfilled such as: 1) the bulk solid behaviour during flow has to be described with a realistic constitutive model by taking the effect of pressure and initial void ratio into account, 2) the continuum constitutive model has to be enhanced by a characteristic length of micro-structure in order to obtain mesh-independent results and to properly capture shear localization (width, inclination and spacing), which is a fundamental phenomenon of each granular flow and 3) the excessive distortion of the finite element mesh during silo flow has to be avoided by means of a suitable description of the material motion. We satisfied these three conditions by using: 1) a hypoplastic constitutive model that captures the salient properties of granular bulk materials (e.g. [14–17]), 2) the hypoplastic model was enhanced by a characteristic length of micro-structure in the frame of a non-local theory [14,18] to get objective numerical results (e.g. [8,14,18]) and 3). the material motion was captured with the material point method (MPM) allowing for large mesh deformation (e.g. [19–25]).

The objective of our two-dimensional (2D) plane strain numerical investigations was to provide an accurate representation of quasi-static granular flow in a model silo with parallel walls and slowly movable bottom with a constant velocity using the explicit MPM [25] and a non-local hypoplastic model [18] by taking shear localization into account. The current paper is numerically oriented. The focus was on the development of shear zones during granular silo flow which are an inherent property of all deforming granular materials. The shear zones are crucial for both the wall pressure distribution and flow pattern in silos [8,10]. In the calculations, the location and width of the silo outlet, wall roughness and initial void ratio of granular material were varied. The paper consists of three numerical parts. The first part presents some MPM results of various simple geotechnical element tests (triaxial compression and shear with free dilatancy) carried out with a local hypoplastic material model to demonstrate its capability to realistically capture the most salient properties of granular

* Corresponding author.
Email addresses: jakub.krzyzanowski@pg.edu.pl (J. Krzyżanowski); tejchmk@pg.edu.pl (J. Tejchman); wojciech.solowski@aalto.fi (W. Sołowski); michal.wojcik@pg.edu.pl (M. Wójcik)

https://doi.org/10.1016/j.powtec.2020.10.001
0032-5910/ © 2020.

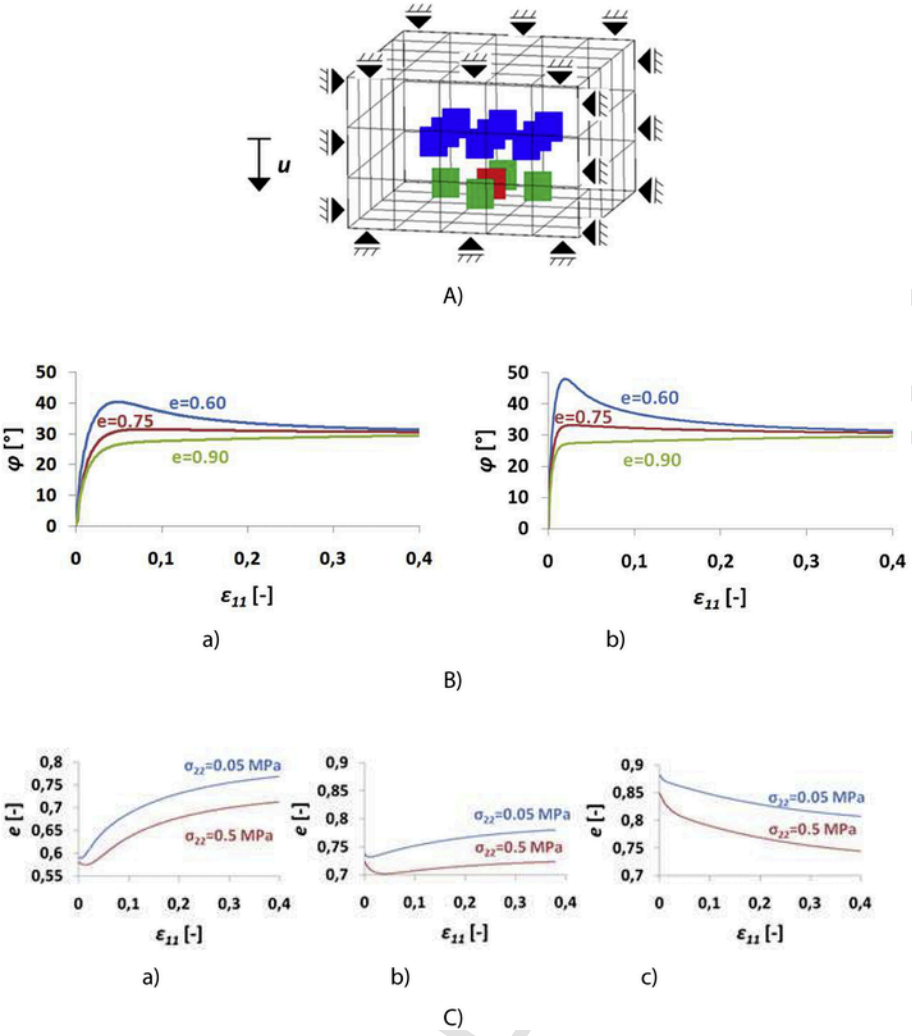

Fig. 1. MPM element test calculations for triaxial compression: A) MPM grid and B) evolution of mobilized internal friction angle ϕ and C) void ratio e versus vertical normal strain ε_{11} for different initial void ratios of sand (a) $e_o = 0.60$, b) $e_o = 0.75$ and c) $e_o = 0.90$) and lateral pressures ($\sigma_{22} = 500$ kPa and $\sigma_{22} = 50$ kPa).

materials (effect of initial void ratio and pressure). In the second part, some numerical results with a non-local hypoplastic constitutive model based on MPM are presented as compared to two different laboratory tests on Karlsruhe sand to show its capability to reproduce objective shear localization during granular flow. The calculations were performed for quasi-static plane strain compression [26] and quasi-static mass flow of with controlled outlet velocity along the entire bottom in a model silo with parallel walls [8,10,27]. The simulation results were directly compared with the corresponding experiments. In the numerical analyzes, initial void ratio of sand and wall roughness were varied. Finally, in the third numerical part, the same approach was used for the same model silo wherein the location and width of the silo outlet were varied (the width of a symmetric/non-symmetric outlet was always smaller than the silo width). Thus, large bulk solid deformation took place. The simulations were aimed at showing the impact of the outlet location and width on the evolution and distribution of shear zones in sand and wall pressures (by varying also the wall roughness and initial void ratio of sand). In calculations with the outlet at the wall, the phenomenon of multiply branching of shear zones occurred in initially dense sand. Such comprehensive shear zone simulations during granular flow in silos were not carried out yet.

In our previous paper concerning the simulations of confined granular mass flow with a slowly movable bottom in a model bin using the finite element method (FEM) [10], we employed the same constitutive model for describing granular flow but within a different motion's description, namely the so-called uncoupled Arbitrary Lagrangian-Eulerian (ALE) formulation (accessible in the program Abaqus/Explicit [28]). The ALE formulation was thus proved to be successful in describing silo flow, however, it failed during silo flow with inserts due to the convergence problems caused by the presence of 'empty' finite elements under fixed inserts. This fact was a motivation for us to use now another description of motion during silo flow - MPM wherein this drawback does not happen. The novel elements of the paper are: 1) a careful calibration of the MPM approach based on two different laboratory experiments (plane strain compression and granular mass silo flow), 2) use of MPM for investigating wall and internal shear zones during granular flow and 3) investigations of the effect of the outlet location and outlet width on the evolution of shear localization and wall pressures for the different wall roughness and initial void ratio of the solid.

MPM was used to different problems concerning the flow behaviour of granular materials (e.g. [29–33]). The granular silo flow was also numerically investigated using MPM [34–38], based mainly on

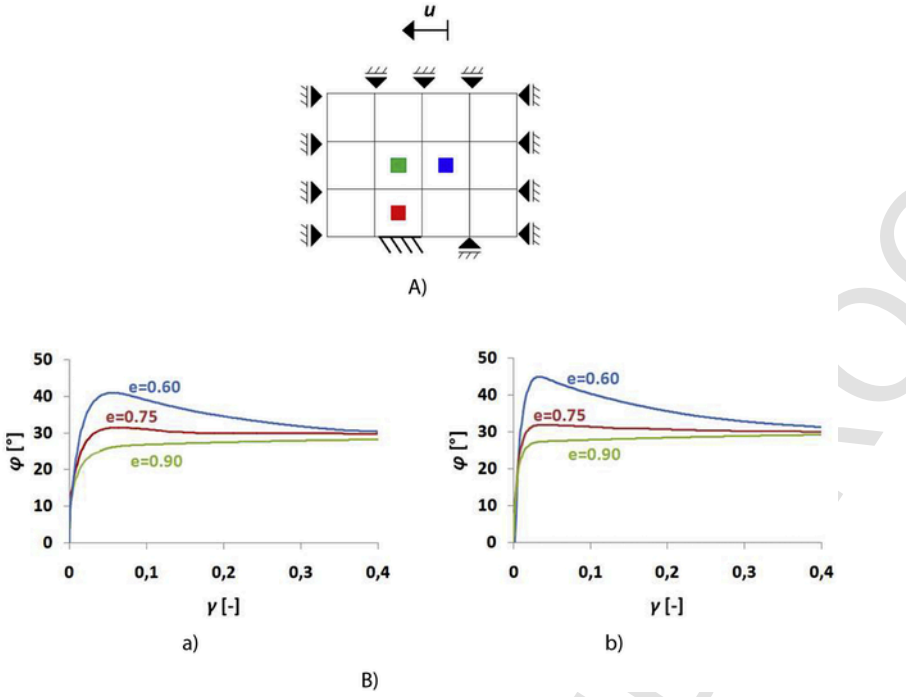

Fig. 2. MPM element test calculations for simple shear with free dilatancy: A) MPM grid and B) evolution of mobilized internal friction angle ϕ versus shear strain γ for different initial void ratios of sand ($e_o = 0.60$, $e_o = 0.75$ and $e_o = 0.90$) and lateral pressures (a) $\sigma_{22} = 200$ kPa and (b) $\sigma_{22} = 50$ kPa).

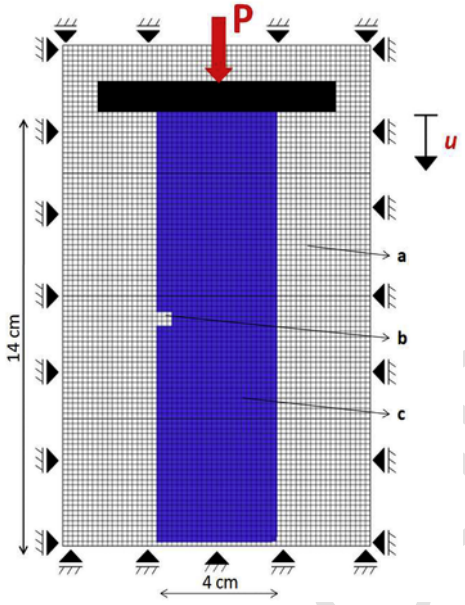

Fig. 3. Boundary conditions, specimen geometry and computational MPM grid: a) computational mesh, b) imperfection and c) granular specimen (P - vertical top force, u - vertical top displacement.

elasto-plastic and hypoplastic constitutive models without a characteristic length of micro-structure. The method proved to be effective to describe the entire emptying process in silos. However, the numerical results were dependent upon the number of material points. In [39], MPM was applied to granular flow in a silo for the elastic-perfectly plastic material model enhanced by viscosity. The viscoplastic regularization is solely effective if a granular flow velocity is relatively high. The granular silo flow was also modelled in Eulerian coordinates (e.g. [40–45]), mixed Lagrangian-Eulerian coordinates (e.g. [10,46,47]) and Lagrangian coordinates [8,48–50]. In addition, the granular silo flow was simulated with DEM (e.g. ([44,51–54]) and cellular automata (CA) (e.g. [55,56]). Because of its heavy computational demand, the application of DEM and CA is limited to relatively small silos.

The paper is structured as follows. After Introduction (Section 1), a hypoplastic constitutive model and its non-local enrichment are shortly summarized in Section 2. The numerical framework of MPM is given in Section 3. Sections 4 and 5 include the MPM results of element tests and plane strain compression. The MPM results on granular silo flow with controlled outlet velocity with key findings are discussed in Sections 6 (the case of the outlet width equal to the silo width) and 7 (the cases of the outlet width smaller than the silo width and the non-symmetric outlet location with respect to a symmetry axis). We summarize and conclude in Section 8.

2. Hypoplastic constitutive model for granular materials

Local hypoplastic constitutive models for granular materials were comprehensively described in several earlier publications (e.g. [9,14–17]). Below, their most important basic properties are summarized. In hypoplastic constitutive models [13–15], the stress rate tensor depends on current stress, strain rate and void ratio using linear and non-linear isotropic tensorial functions. The models are incrementally non-linear in the deformation rate. They reproduce the salient properties of granular materials such as e.g. non-linear stress-strain relationship, dilatant and contractant volumetric change, stress level dependence, void ratio dependence, deformation direction dependence and strain softening. They include the critical states (characteristic for granular materials) at which the granulates continuously deform at the constant stress and void ratio. They do not assume in advance the coaxiality (the coincidence of the direction of the principal stresses and principal plastic strain increments) and stress-dilatancy rule [57].

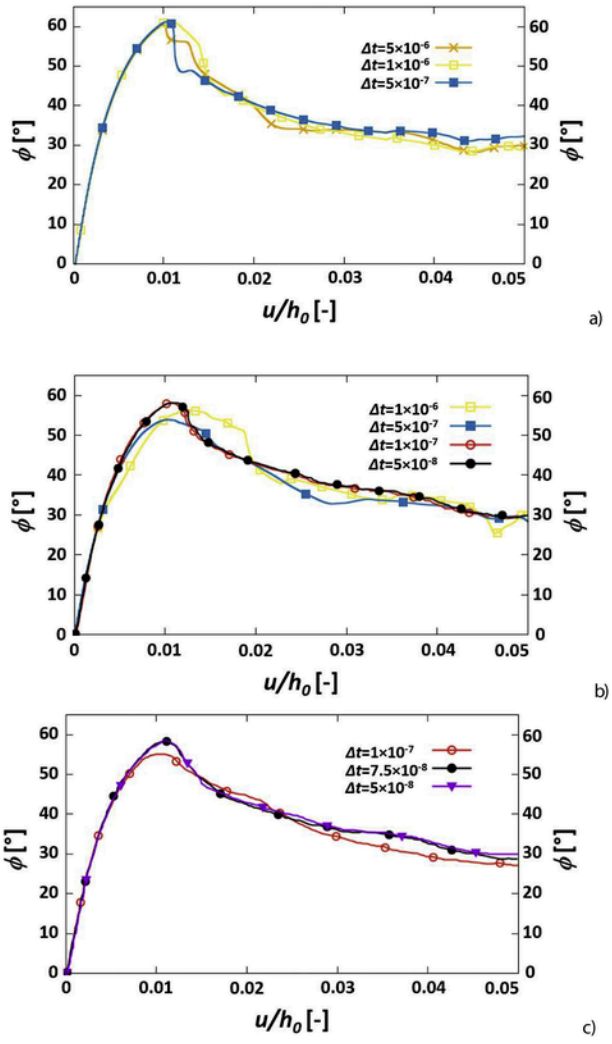

Fig. 4. Evolution of mobilized internal friction angle ϕ versus vertical strain u/h_o during plane strain compression using MPM ($p=50$ kPa, $e_o=0.55$ and $l_c=1.5$ mm) for different material point grids and time steps Δt: a) grid 16×56 (grid size 2.5×2.5 mm^2), b) grid 24×84 (grid size 1.66×1.66 mm^2) and c) grid 32×112 (grid size 1.25×1.25 mm^2).

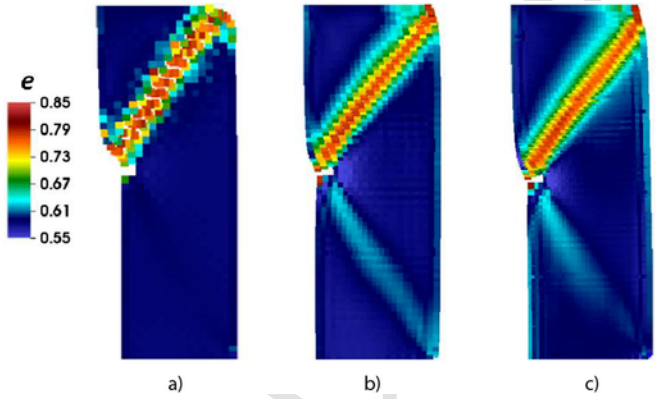

Fig. 5. Deformed specimens for $u/h_o=5\%$ with distribution of void ratio e during plane strain compression using MPM for different material point grids ($\Delta t=1\times10^{-7}$): a) grid 16×56 (grid size 2.5×2.5 mm^2), b) grid 24×84 (grid size 1.66×1.66 mm^2) and c) grid 32×112 (grid size 1.25×1.25 mm^2).

The failure surface and flow rule emerge as by-products [58] and are also not prescribed. Hypoplastic models are characterized by simple formulation and procedure for determining material parameters with standard laboratory tests. Thus, the material parameters can be related to the granulometric properties of granular materials, such as grain size distribution curve, shape, angularity and hardness of grains [57]. Only one single set of material parameters is needed being valid for a wide range of pressures and densities. Hypoplastic models correctly perform for monotonous deformation paths due to grain skeleton rearrangements. However, they show a shortcoming for deformation with small amplitudes (so-called 'ratcheting' [60]). Based on preliminary calculations, the hypoplastic constitutive model was not extended by the intergranular strain to avoid ratcheting [60] and dynamic viscosity [61] due to slow quasi-static silo flow assumed in numerical simulation.

The equations of the local hypoplastic constitutive law used in our calculations [16] are listed in Appendix (Eqs.A1-A10) [16]. The calibration procedure of hypoplastic material parameters for different sands was given by Bauer [16] and Herle and Gudehus [59]. The hypoplastic constitutive model requires eight material parameters: e_{i0}, e_{d0}, e_{c0}, ϕ_c, h_s, β, n and α (Appendix 'A'). They are valid for a pressure range of $1\,\text{kPa}<p_s<1000\,\text{kPa}$. For problems involving shear localization, the constitutive model was enriched by a characteristic length of micro-structure to regularize the boundary value problem and to achieve objective and convergent numerical solutions [9]. We used a non-local approach [9,18,62] to include a characteristic length of micro-structure for properly calculating shear zones (width, shape and spacing). Our hypoplastic MPM calculations were carried out with a non-local norm of the deformation rate d^*

$$d^*(\boldsymbol{x}) = \frac{\int_V \omega(\|\boldsymbol{x}-\boldsymbol{\xi}\|)\, d(\boldsymbol{\xi})\, d\boldsymbol{\xi}}{\int_V \omega(\|\boldsymbol{x}-\boldsymbol{\xi}\|)\, d\boldsymbol{\xi}} \tag{1}$$

with

$$\omega(r) = \frac{1}{l_c\sqrt{\pi}} e^{-(r/l_c)^2} \tag{2}$$

where d^* - the non-local norm of the deformation rate, $d=\|D_s\|$ - the local norm of the deformation rate (Eq. A1 in Appendix 'A'), V - the body volume, $\boldsymbol{x}$ - the coordinates of the considered (actual) point, $\boldsymbol{\xi}$ - the coordinates of the surrounding points, ω - the weighting function, l_c - the characteristic length of micro-structure and r the distance between two points. The parameter l_c is usually determined with an inverse identification process of experimental data [9]. For Karlsruhe sand, the characteristic length was about $l_c=1.5$ mm ($3\times d_{50}$) [9,10]. The MPM simulations were carried out with the following set of the material constants for so-called Karlsruhe sand (mean grain diameter $d_{50}=0.5$ mm): $e_{i0}=1.3$, $e_{d0}=0.51$, $e_{c0}=0.82$, $\phi_c=30^o$, $h_s=190$ MPa, $\beta=1$, $n=0.5$, $\alpha=0.3$ [16] and $l_c=1.5$ mm [10].

3. Material point method (MPM)

MPM calculations were carried out with the Uintah open-source software [23]. The non-local hypoplastic model was implemented into Uintah.

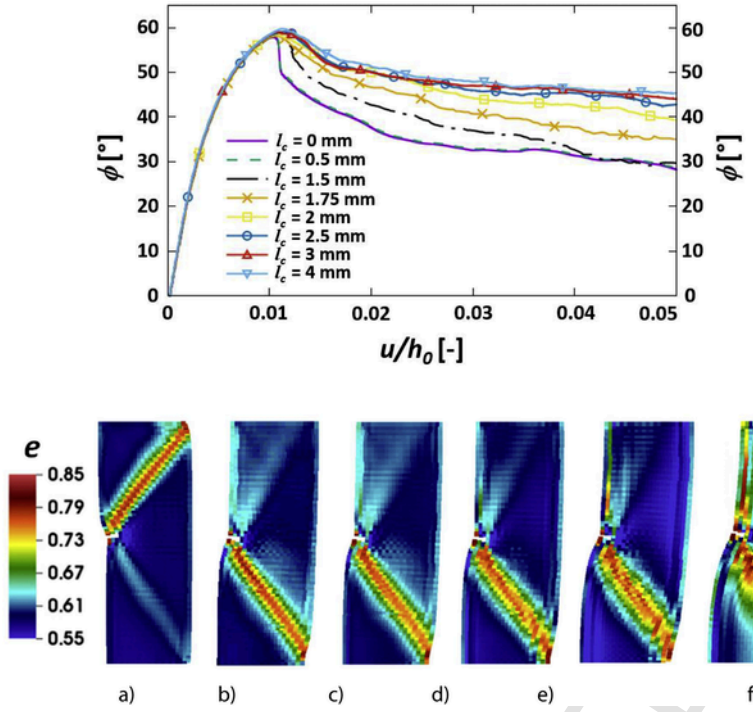

Fig. 6. Plane strain compression using MPM: evolution of mobilized internal friction angle ϕ versus vertical strain u/h_o (p=50 kPa and e_o=0.55) and deformed specimens for u/h_o=5.0% with distribution of void ratio e for different characteristic length l_c=0–4 mm (a) l_c=1.5 mm, b) l_c=1.75 mm, c) l_c=2 mm, d) l_c=2.5 mm, e) l_c=3 mm and f) l_c=4 mm).

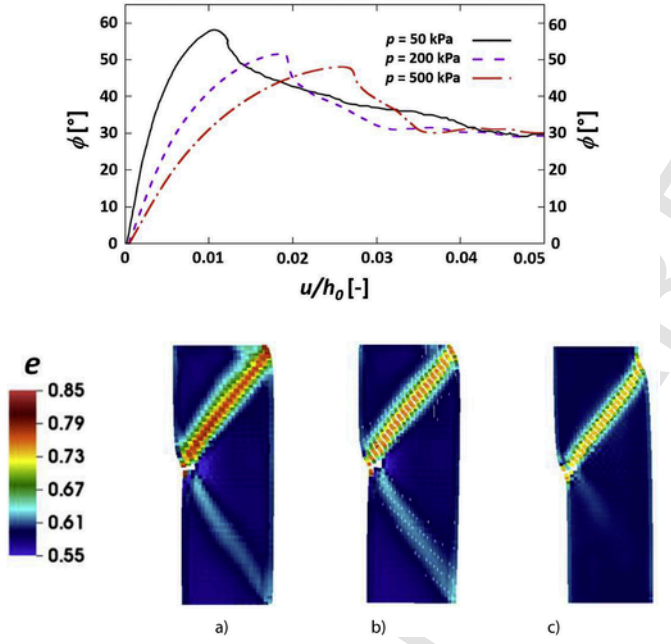

Fig. 7. Plane strain compression using MPM: evolution of mobilized internal friction angle ϕ versus vertical strain u/h_o (e_o=0.55, l_c=1.5 mm) and deformed specimens for u/h_o=5% with distribution of void ratio e for different lateral pressure (a) p=50 kPa, b) p=200 kPa and c) p=500 kPa).

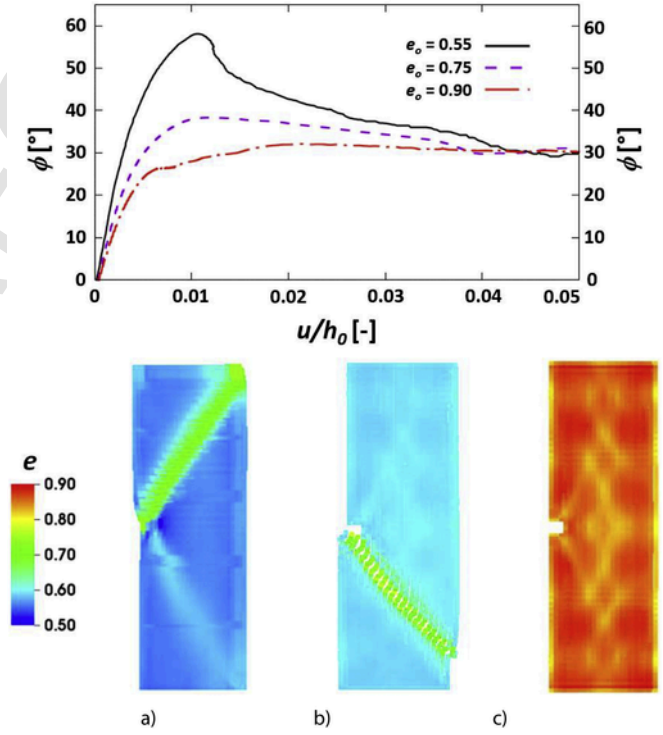

Fig. 8. Plane strain compression using MPM: evolution of mobilized internal friction angle ϕ versus vertical strain u/h_o (p=50 kPa, l_c=1.5 mm) and deformed specimens for u/h_o=5% with distribution of void ratio e for different initial void ratio e_o (a) e_o=0.55, b) e_o=0.75 and c) e_o=0.90).

3.1. Standard formulation

The material point method (MPM) is a powerful numerical tool in dynamic simulations of large deformation/distortion problems [19–23]. It is very similar to FEM but overcomes difficulties associated with large mesh distortion since it uses an arbitrary computational mesh to trace the history of state variables for body particles during the entire deformation process. The method may be classified as a

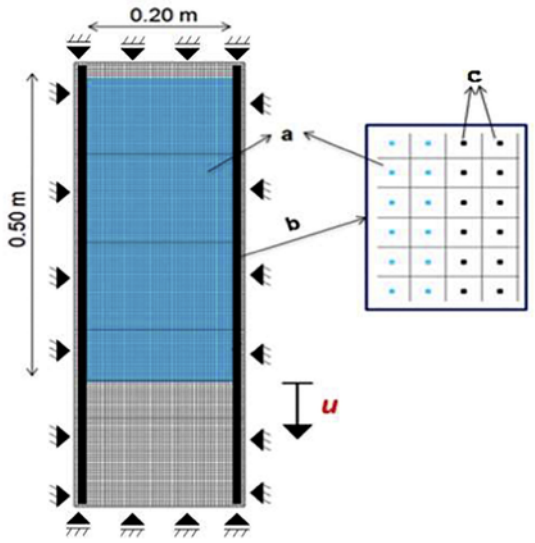

Fig. 9. MPM model of silo with parallel walls (height $h = 0.5$ m and width $b = 0.2$ m) with constant outlet velocity along bottom: a) bulk solid, b) zoom on material point grid of silo fill and c) zoom on material point grid of rigid wall (u - constant bottom displacement).

meshless method. For each time increment, the MPM calculations include 2 main steps: 1) Lagrangian step and 2) convective step. In step '1', the computational mesh deforms together with the material. All spatial and temporal state variables are calculated for each material point by using conventional shape functions and nodal parameters defined on the computational mesh. In step '2' (convective step), the velocity field is mapped from material points to the computational grid that can remain at the same position as at the beginning of the time increment. The important differences with FEM are: a) the mass matrix varies with time, b) the gradient, stress and strain are evaluated at material points that can move and c) the point masses appear in internal and external force vectors.

The continuum is discretized by a grid composed of material points (cells) whose motion is traced by a background mesh which may be regular. The equation of the virtual work formulated for MPM is [19–21].

$$\int_{\Omega} \varrho \left(a_i w_i + \frac{1}{\varrho} \sigma_{ij} w_{ij} \right) dx = \int_{\Omega} \varrho b_i w_i dx + \int_{\Gamma_\sigma} t_i w_i \, ds + \int_{\Gamma_c} \sigma_{ij} n_j w_i ds, \tag{3}$$

where Ω describes the region of the analyzed continuum at time t, $\partial\Omega$ is the boundary of the region Ω where stresses Γ_σ and contacts Γ_c are given, $\boldsymbol{\sigma}_{ij}$ and $\boldsymbol{t}_i$ are the Cauchy stress tensor and vector, $\boldsymbol{b}_i$ denotes the vector of body forces, $\boldsymbol{n}_j$ stands for the unit vector outwardly normal to the boundary region $\partial\Omega$, ϱ represents the mass density, $\boldsymbol{a}_i$ is the vector of accelerations and $\boldsymbol{w}_i$ is the test (weighting) function. The entire mass of a continuum subregion is concentrated in a representative material point. The density field around each material point is expressed as [19]:

$$\varrho(x) = \sum_{P=1}^{N} \boldsymbol{M}_P \delta \left(\boldsymbol{x} - \boldsymbol{X}_P \right) \tag{4}$$

where M_P - the mass and $\boldsymbol{X}_P$ - the position of the P^{th} material point, $\delta(x)$ - the Dirac delta function with dimension of the volume inverse and N - the point number. After applying Eq. (4) and using the standard finite element approximation for the fields $\boldsymbol{a}_i$ and $\boldsymbol{w}_i$, the following system of equations is obtained

$$\boldsymbol{Ma} = \boldsymbol{F}_{int} - \boldsymbol{F}_{ext}, \tag{5}$$

where

$$\boldsymbol{M} = \sum_{P=1}^{N} M_P \boldsymbol{N}^t \left(\boldsymbol{X}_P \right) \boldsymbol{N} \left(\boldsymbol{X}_P \right) \quad or \quad \boldsymbol{M} = \sum_{P=1}^{N} M_P \boldsymbol{N} \left(\boldsymbol{X}_P \right), \tag{6}$$

and

$$\left(\boldsymbol{F}^t \right)_{int} = \sum_{P=1}^{N} M_P \boldsymbol{G} \left(\boldsymbol{X}_P \right) \frac{\boldsymbol{s}}{\rho} \left(\boldsymbol{X}_P \right) \tag{7}$$

The mass $\boldsymbol{M}$ is the consistent or lumped mass matrix, $\boldsymbol{F}_{int}$ is the vector of nodal internal forces, $\boldsymbol{G}(\boldsymbol{X}_P)$ is the gradient of the shape function evaluated at $\boldsymbol{X}_P$, $\boldsymbol{s}$ is the particle stress tensor and $\boldsymbol{F}_{ext}$ is the vector of nodal external forces. Most standard MPM implementations use piecewise-linear basis functions $\boldsymbol{N}$ due to their implementation ease. The full explicit algorithm was given in [19]. There exist also some implicit formulations of MPM [63–68].

3.2. Improved MPM formulations

An improved variant of MPM called the generalized interpolation material point (GIMP) method may be used [69,70] in the open-source program Uintah to improve the accuracy, stability and robustness of simulations through the introduction of particle characteristic functions which have a positive smoothing effect on grid basis functions. GIMP replaces the Kronecker delta (Eq. 4) with a general particle characteristic function centred at the particle position. Any material point and property may be computed at the point $\boldsymbol{x}$ as

$$f(\boldsymbol{X}) = \sum_{P=1}^{N} f_P \chi_P (\boldsymbol{X}) \tag{8}$$

where χ_P - the particle characteristic function. Thus e.g. the mass corresponding to the point is smeared over a constant volume. The nodal values ('n') for the quantity f, known at material points, are defined as

$$f_n = \sum_{P=1}^{N} f_P \overline{N} \tag{9}$$

with the weighting function (V_P - the material point volume) using the particle spacing as the width of the particle characteristic function.

$$\overline{N} = \frac{1}{V_P} \int_{\Omega} \chi_P (\boldsymbol{X}) \boldsymbol{N} (\boldsymbol{X}) dx \tag{10}$$

The equations with the gradients are similarly modified to use a gradient weighting function. In GIMP, the standard piecewise-linear grid basis functions and piecewise-constant particle characteristic functions are applied. In traditional MPM, boundary conditions only need to be applied to those nodes which coincide with the extents of

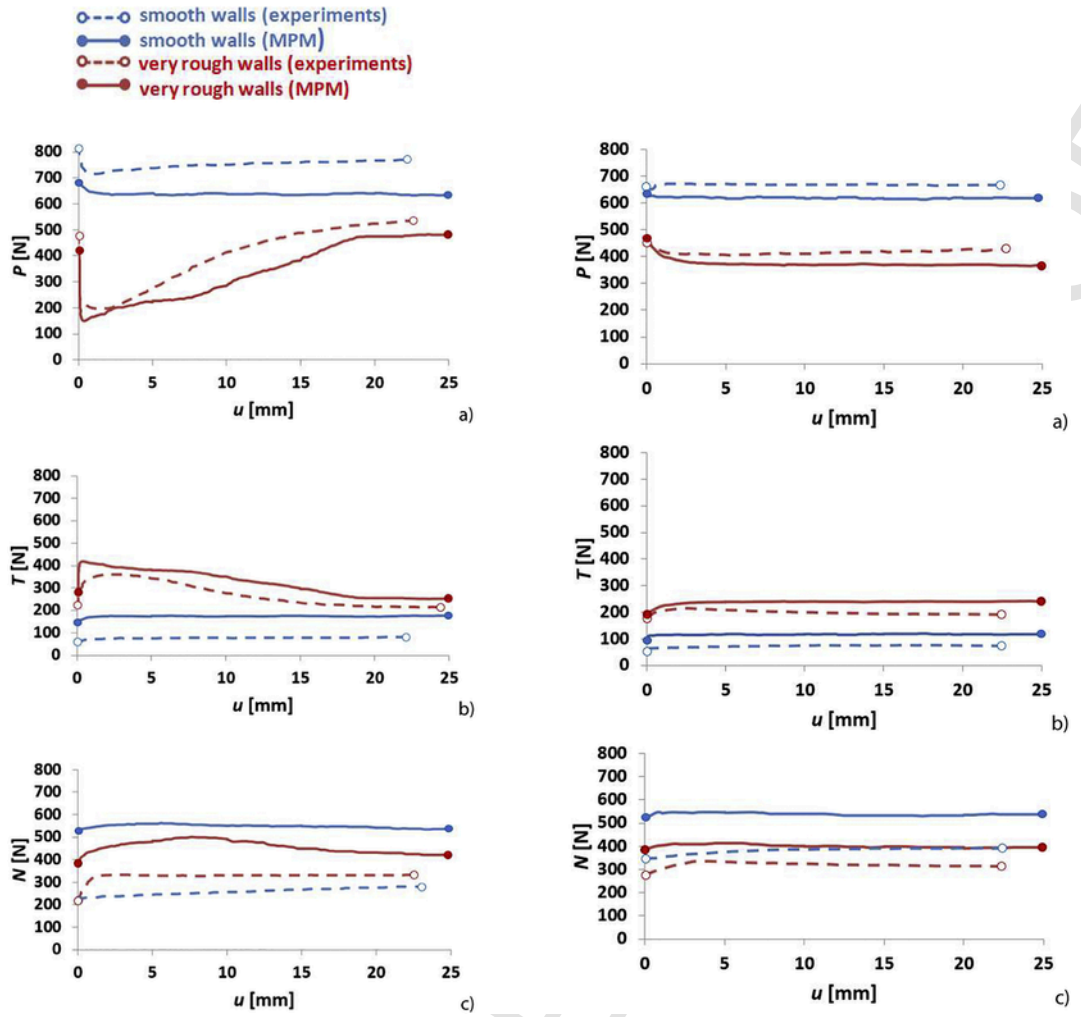

Fig. 10. Evolution of experimental and numerical resultant forces after bottom displacement u in model silo for: A) initially dense sand ($e_o = 0.60$) and B) initially loose sand ($e_o = 0.90$) (a) resultant bottom force P, b) resultant wall friction force T and c) resultant wall normal force N).

the computational domain. In GIMP, the particles may be influenced by nodes that lie outside of the simulation domain to reduce the numerical noise associated with particles crossing grid boundaries [23]. In contrast to a standard formulation, there exists a computational domain in GIMP that can undergo normal deformation, lengthening or shortening (called cpGIMP) or constitutes a constant area around a material point (called uGIMP). The effective averages of the basis function and its gradient over the particle domain are

$$\varphi_{ip} = \frac{1}{V_p}\int_{\Omega} \chi_P\left(\boldsymbol{x} - \boldsymbol{X}_P\right) S_i\left(x\right) dx \tag{11}$$

$$\nabla\varphi_{ip} = \frac{1}{V_p}\int_{\Omega} \chi_P\left(\boldsymbol{x} - \boldsymbol{X}_P\right) \nabla S_i\left(x\right) dx \tag{12}$$

Uintah gives also the opportunity to use another improved variant of MPM called CPDI [71] (convected particle domain interpolation) wherein an additional computational domain exists subjected to shear deformation. Moreover, CPDI uses a modified shape function gradient that is continuous at cell borders. The particle domains are treated as rectangles with uGIMP and cpGIMP. Under shear deformation, the particle domains should become parallelograms which is not possible in GIMP directly. In CPDI, the alternative grid basis functions are constructed to be an interpolation of standard grid basis functions at four corners of each particle domain for calculations of the integrals in Eqs.11 and 12 (when the particle domains became parallelograms)

$$S_i^{app}\left(x\right) = \sum_{\alpha=1}^{4} Q_\alpha^p\left(\boldsymbol{x}\right) S_i\left(\boldsymbol{x}_\alpha^p\right) \tag{13}$$

in which Q_α^p is the standard FE 4-node (Q4) shape function related to the α^{th} corner of the domain corresponding to the particle p and $\boldsymbol{x}_\alpha^p$ is the corner position.

3.3. Errors and stability of MPM

MPM is still in development with no formal proof of convergence available. The method is being constantly improved with recent developments showing a consistent rate of convergence [72] and strategies to deal with identified errors. An overview of some of the method errors is given below.

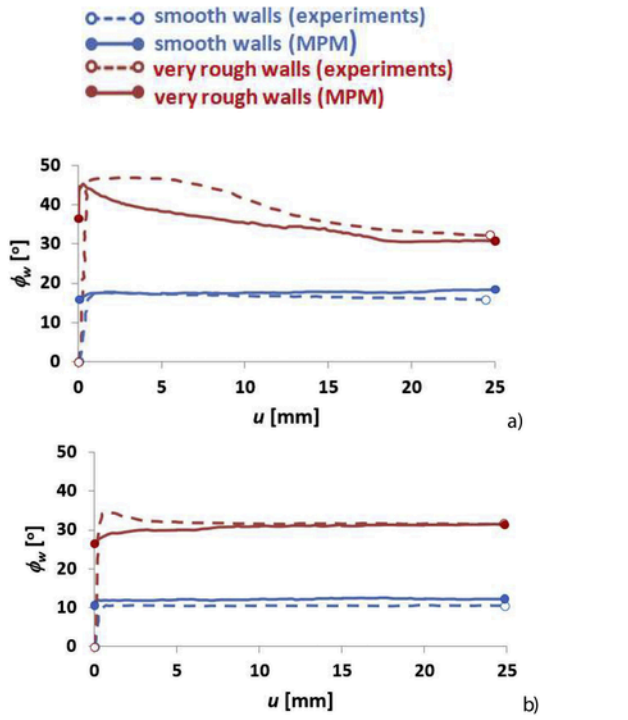

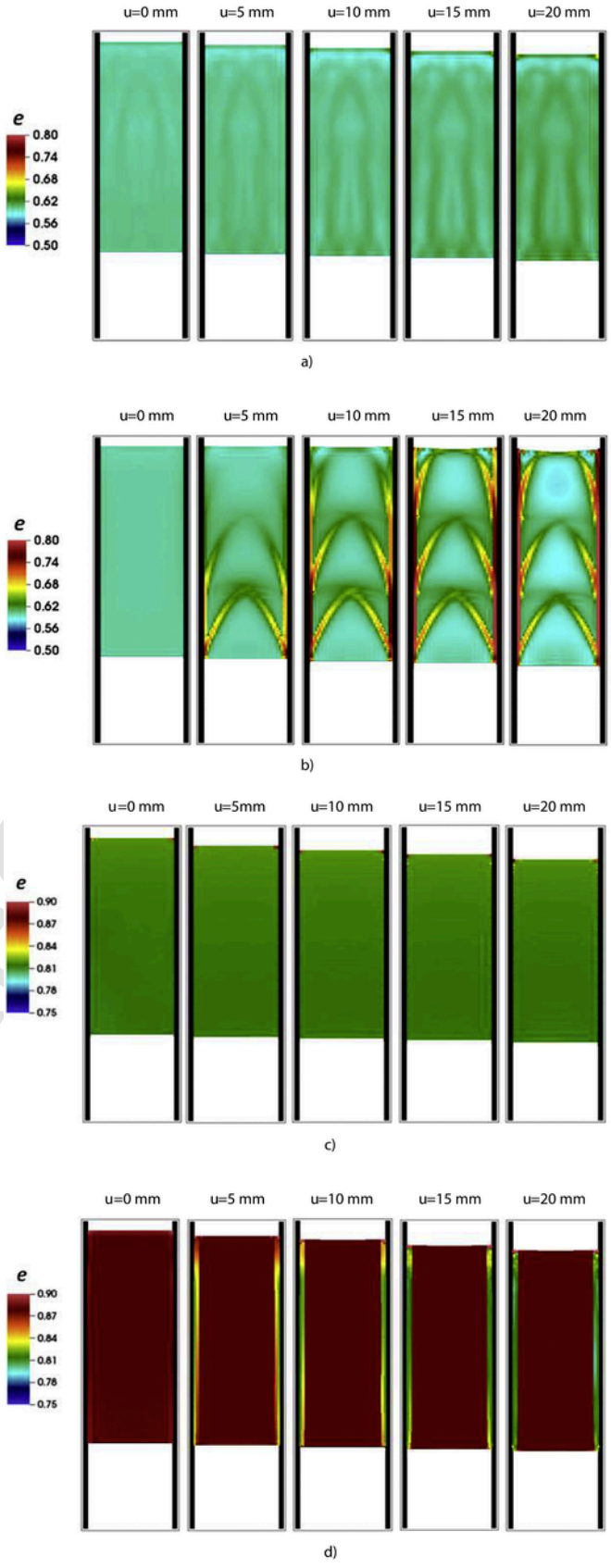

Fig. 11. Evolution of the experimental and numerical mobilized resultant wall friction angle $\varphi_w = \arctan(T/N)$ after bottom displacement u in model silo: a) initially dense sand ($e_o = 0.60$) and a) initially loose sand ($e_o = 0.90$) (T - resultant wall friction force and N - resultant wall normal force).

3.3.1. Cell-crossing errors

Cell-crossing instabilities reduce the accuracy of the standard formulation of MPM. They are caused by a discontinuous gradient of weighting functions that results in a sudden change of the stress when material points move to new cells. They can be mitigated by using a smooth gradient of weighting functions (as in GIMP).

3.3.2. Quadrature and projection errors

Quadrature errors in MPM are due to the first-order integration of field quantities (density, stress) in the background grid [73]. They reduce the accuracy, leading to a reduction of the spatial convergence rate. They can be reduced by using higher-order weighting functions (as in GIMP). MPM uses a first-order Shepard interpolation [74] to project velocities from material points to grid nodes. A velocity gradient enhancement reduces velocity projection errors [75].

3.3.3. Null-space errors

Null-space errors are caused by a mismatch between material points and grid nodes when Fourier modes in material points with wavelengths shorter than the grid spacing are indistinguishable at grid nodes [76]. This error may be reduced by a null-space filter [77–79].

3.3.4. Non-linear instability

In the explicit MPM formulation, the Courant-Friedrichs-Levy (CFL) condition is commonly used to determine the critical time step for numerical solutions [80]. However, this condition which is used for linear stability analyses does not always ensure a stable non-linear solution in MPM [81]. Jiang et al. [82] selected the critical time step considering the maximum velocity of material points. Berzins [83] proposed a critical time step using a non-linear stability analysis.

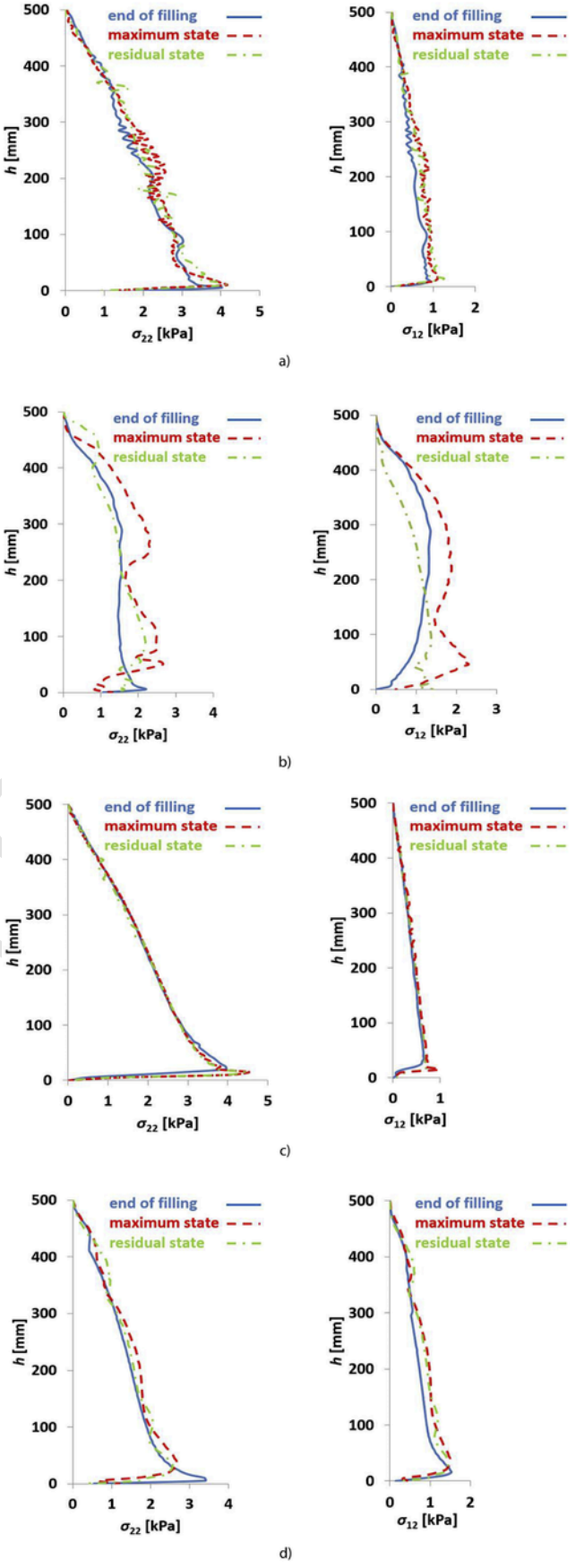

Fig. 12. Numerical evolution of void ratio in sand after bottom displacement u in model silos depending upon initial void ratio and wall roughness: a) initially dense sand ($e_o = 0.60$) and smooth walls, b) initially dense sand ($e_o = 0.60$) and very rough walls, a) initially loose sand ($e_o = 0.90$) and smooth walls and d) initially loose sand ($e_o = 0.90$) and very rough walls.

4. Basic element tests

Initially, some basic element tests on sand (oedometric compression, plane strain compression, triaxial compression, shear with constant and free dilatancy) were carried out with a local hypoplastic model using MPM. The results of a triaxial compression test and shear test with free dilatancy were shown. Regular computational grids compose of quadrilateral elements were always applied. Hypoplastic calculations were carried out for the red points in Figs. 1A and 2A. The green points were introduced to consider pressure and the blue points to discretize the rigid elements in Figs. 1A and 2A.

4.1. Triaxial compression

The evolution of both the mobilized internal friction angle φ (calculated with principal stresses from the Mohr's equation) and void ratio e against the vertical strain ε_{11} is shown in Fig. 1B and C for the different lateral pressure σ_{22} and initial void ratio of sand e_o. The calculated peak internal friction angle φ^{peak} realistically increased with decreasing initial void ratio and lateral pressure. The residual internal friction angle φ_{res} was always about 30°. The material dilatancy or contractancy increased/decreased by reducing lateral pressure in initially dense/loose sands.

4.2. Simple shear with free dilatancy

Fig. 2 describes the evolution of the mobilized internal friction angle φ for the different e_o and normal pressure σ_{22} for shear with free dilatancy where a smooth top boundary freely moved in a vertical direction. The peak internal friction angle φ^{peak} again increased with decreasing initial void ratio. The residual internal friction angle φ_{res} was again about 30°.

5. Plane strain compression

The sand specimen under plane strain conditions was numerically simulated with a size of $140 \times 40\,mm^2$ ($h \times b$) as in the experiments by Vardoulakis [26,84] and Vardoulakis et al. [85]. The constant vertical displacement was slowly prescribed along the top boundary to enforce compressive deformation. The horizontal displacements along horizontal boundaries were free (corresponded to ideally smooth boundaries). To preserve the specimen stability, the mid-point at the specimen bottom was fixed. The quadrilateral MPM grid was used (Fig. 3) with one material point per grid cell. Gravity was taken into account. For inducing a shear zone, a small imperfect element of a size $5 \times 5\,mm^2$ with a higher void ratio ($e_o = 0.91$) was placed at the specimen mid-height (left side). The initial void ratio of sand was $e_o = 0.55$, 0.75 and 0.90 and the lateral (confining) pressure was $p = 50\,kPa$, 200 kPa and 500 kPa. The characteristic length l_c varied between 0 mm and 4 mm. The calculations were carried out using the CPDI version of MPM (Section 4).

5.1. Effect of time increment and material point mesh

MPM calculations were performed with a different time step $\Delta t = 5 \times 10^{-8}$ - 5×10^{-6} s (applied in the explicit procedure of time inte-

gration of dynamic equations) and a different material point grid: 16×56, 24×84 and 32×112. The grids corresponded to the cell size of $2.5\times2.5\,mm^2$, $1.66\times1.66\,mm^2$ and $1.25\times1.25\,mm^2$, respectively. The evolution of the mobilized internal friction angle ϕ against the vertical strain u/h_o is shown in Fig. 4 for four different time steps and three different numbers of material points ($p=50$ kPa, $e_o=0.55$ and $l_c=1.5$ mm). The optimum time increment was found to be $\Delta t=1\times10^{-7}$ for the mesh composed of 24×84 material points (cell size was $1.66\times1.66\,mm^2$). Fig. 5 demonstrates the effect of the size of the material point mesh on shear localization. The material point mesh dependence did not occur for the grid 24×84 (element size $1.66\times1.66\,mm^2$) and the grid 32×112 (grid size $1.25\times1.25\,mm^2$).

5.2. Effect of characteristic length

The various characteristic lengths were tested, ranging from $l_c=0$ mm up to $l_c=4$ mm (Fig. 6). The initial void ratio was set on $e_o=0.55$ and the lateral pressure on $p=50$ kPa. Similarly, as in real experiments [26,84,85], the initially dense specimen showed an asymptotic behaviour; it exhibited initially small elasticity, hardening, reached a peak, gradually softened and dilated approaching a residual (critical) state. Both the maximum internal friction angles ϕ^{peak} and residual internal friction angle ϕ_{res} increased with growing l_c. For the value of $l_c=1.5$ mm, the value of $\phi^{peak}=55^o$ for the strain of $u/h_o=1.2\%$ and was close to $\phi_{res}=30^o$ for $u/h_o=4.0\%$. For $l_c=4$ mm, $\phi^{peak}=60^o$ and $\phi_{res}=45^o$.

During deformation, a clear internal inclined shear zone occurred inside the sand specimen as in the experiment [26]. It was marked by shear strain and volume increase. First, two shear zones occurred starting from the imperfection. Later a single shear dilatant zone dominated that was created just before reaching the peak stress. For $l_c=1.5$ mm, the final inclined shear zone developed in the upper part of the specimen, whereas for $l_c>1.5$ mm, it was located in the lower specimen region. The thickness of the shear zone was determined based on the distribution of void ratio e by assuming $e\geq0.70$. The thickness of the inclined dilatant shear zone was on average in the residual state about $t_s=7.5\,mm=5\times l_c=15\times d_{50}$ based on the dilatant region and its inclination against the bottom was about 55° as in the experiment [26].

5.3. Effect of lateral pressure and initial void ratio

The influence of the lateral pressure $p=50$–500 kPa on the mobilized internal friction angle and shear localization is shown in Fig. 7 ($e_o=0.55$ and $l_c=1.5$ mm). Fig. 8 describes the influence of the initial void ratio $e_o=0.55$–0.90 on the mobilized internal friction angle and shear localization ($p=50$ kPa and $l_c=1.5$ mm).

As the lateral pressure p increased, the peak internal friction angle decreased: $\phi^{peak}=55^o$ for 50 kPa, $\phi^{peak}=50^o$ for 200 kPa and $\phi^{peak}=47^o$ for 500 kPa. As the initial void ratio increased, the peak internal friction angle decreased: $\phi^{peak}=55^o$ for $e_o=0.55$, $\phi^{peak}=40^o$ for $e_o=0.75$ and $\phi^{peak}=30^o$ for $e_o=0.90$. The residual internal friction angle remained always the same. With increasing p, the thickness of the shear zone t_s slightly increased: $t_s=5\times l_c$ for $p=50$ kPa, $t_s=6.33\times l_c$ for $p=200$ kPa and $t_s=7.33\times l_c$ for $p=500$ kPa. With growing e_o up to $e_o=0.75$ the thickness of the shear zone t_s increased from $t_s=5\times l_c$ for $e_o=0.55$ up to $t_s=6\times l_c$ for $e_o=0.75$. No shear was observed in an initially loose specimen ($e_o=0.90$) (Fig. 8c). The inclination of the shear zone to the horizontal θ decreased with growing p ($\theta=55^o$ for $p=50$ kPa, $\theta=54^o$ for $p=200$ kPa and $\theta=52^o$ for $p=500$ kPa) and with increasing e_o ($\theta=55^o$ for $e_o=0.55$ and $\theta=50^o$ for $e_o=0.75$). The outcomes were again close to the experiments [24]. They were also in agreement with the numerical results using a micro-polar hypoplastic model within a pure Lagrangian approach [9,86].

Fig. 13. Calculated distribution of wall stresses in model silo (σ_{22} - wall horizontal stress and σ_{12} - wall shear stress) after bottom displacement depending upon initial void ratio and wall roughness: a) initially dense sand ($e_o=0.60$) and smooth walls, b) initially dense sand ($e_o=0.60$) and very rough walls, c) initially loose sand ($e_o=0.90$) and smooth walls and d) initially loose sand ($e_o=0.90$) and very rough walls ('maximum state' corresponds to maximum resultant wall normal force N_{max} and 'residual state' corresponds to residual wall friction angle $\varphi_{w,res}$).

6. Quasi-static mass sand flow with controlled outflow

The experiments in a plane strain model silo with parallel walls of the height $h=0.5$ m and width $b=0.2$ and a slowly moveable bottom [8] were modelled. In numerical calculations, a slow emptying process was induced by lowering the entire silo bottom ($b=0.2$ m) at a constant velocity of $v=0.1$ mm/s. The bottom velocity was small enough to ensure quasi-static sand mass flow. No damping was defined. The grid of material points was 40×100 (Fig. 9). The cell size was 5 mm ($3\times l_c$) and was small enough to obtain mesh-independent results [9]. The parallel silo walls were assumed as rigid. The initially dense ($e_o=0.60$) and initially loose ($e_o=0.90$) sand specimens were assumed in the silo. To model very rough walls, the vertical and horizontal sand displacements were assumed to be zero [9]. For the other wall roughness, the usual Coulomb friction was assumed with a constant wall friction angle $\varphi_w=\arctan(\sigma_{12}^w/\sigma_{22}^w)$ that was equal to the maximum resultant wall friction angle, measured in the model silo experiments (σ_{12}^w – wall shear stress, σ_{22}^w – wall normal stress) (e.g. $\varphi_w=19^o$ for initially dense sand and $\varphi_w=12.3^o$ for initially loose sand) [8,10,26]. The calculations were carried out using GIMP in two steps: 1) gravitational filling of the model silo and 2) uniform lowering the silo bottom with a constant velocity. The filling state was assumed in a simplified way through a linear increase of the material weight prescribed to the entirely pre-filled silo. The calculations were performed for two extreme cases with respect to the initial void ratio e_o and wall roughness r_w. Fig. 10 shows the calculated evolution of the resultant forces (P, T and N) during silo filling and after bottom displacement u for initially dense ($e_o=0.60$) and initially loose sand ($e_o=0.90$) with smooth and very rough walls as compared to the experiments (T - the resultant vertical wall friction force, N - the resultant horizontal wall force and P - the resultant vertical bottom force). The evolution of the resultant mobilized wall friction angle $\varphi_w=\arctan(T/N)$ in experiments and calculations is demonstrated in Fig. 11.

6.1. Evolution of resultant forces

The evolution shapes of the resultant forces P and T and of mobilized wall friction angle $\varphi_w=\arctan(T/N)$ during emptying for smooth and very rough rigid walls (Figs. 10 and 11) are in satisfactory agreement with our both experiments [8] and previous FE calculations [10]. The initial reduction of the force P and initial growth of T was similar to the experimental outcomes. The reduction (P) or growth (T) became stronger with increasing wall roughness and decreasing initial void ratio. After the force P_{min} or T_{max} was reached, the resultant force increased (P) or decreased (T) with very rough walls and next reached its asymptote. This increase (P) or decrease (N) was stronger with initially dense sand (due to high dilatancy) and weaker with initially loose sand. Larger differences between the experimental and numerical values happened for the resultant horizontal wall forces N which always increased after bottom displacement. The cal-

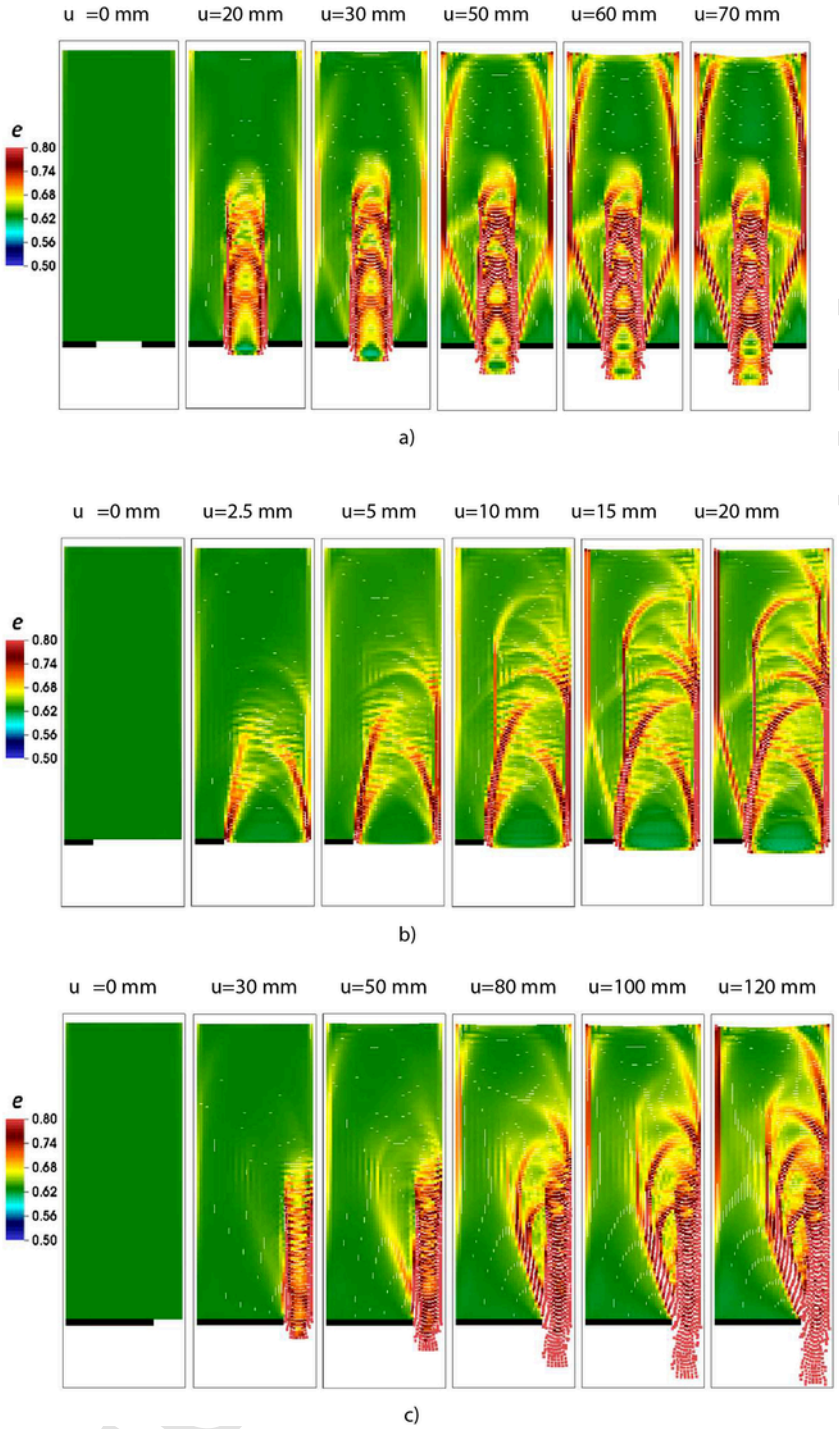

Fig. 14. Calculation evolution of void ratio in initially dense sand ($e_o = 0.60$) after bottom displacement u in model silo with very rough walls for different width and location of outlet: a) symmetric outlet width of 80 mm, b) asymmetric outlet width of 150 mm and c) asymmetric outlet width of 50 mm.

culated maximum values of N in calculations were too high (by factor 1.3–2.5), in particular for smooth walls (Fig. 10Ac and Bc). However, the growths of the wall force N after bottom displacement u were similar in both the calculations and experiments. The differences in values of N_{max} during sand flow are mainly due to wall force discrepancies after silo filling (Fig. 10Ac and Bc), in particular for smooth walls and initially dense sand. More attention must thus be paid to a filling process in calculations (e.g. a more accurate layer-by-layer filling method should improve the results [8,87]). The influence of a filling method on wall pressures was also studied by DEM [88]). The higher the wall roughness and the lower initial void ratio, the higher was the maximum mobilized wall friction angle φ_w^{max} (Fig. 11). For very rough walls and initially dense sand, the mobilized wall friction angle φ_w increased after bottom displacement u reached a peak, decreased and finally approached its asymptote as in the experiment. For remaining cases, the increase of φ_w after bottom displace-

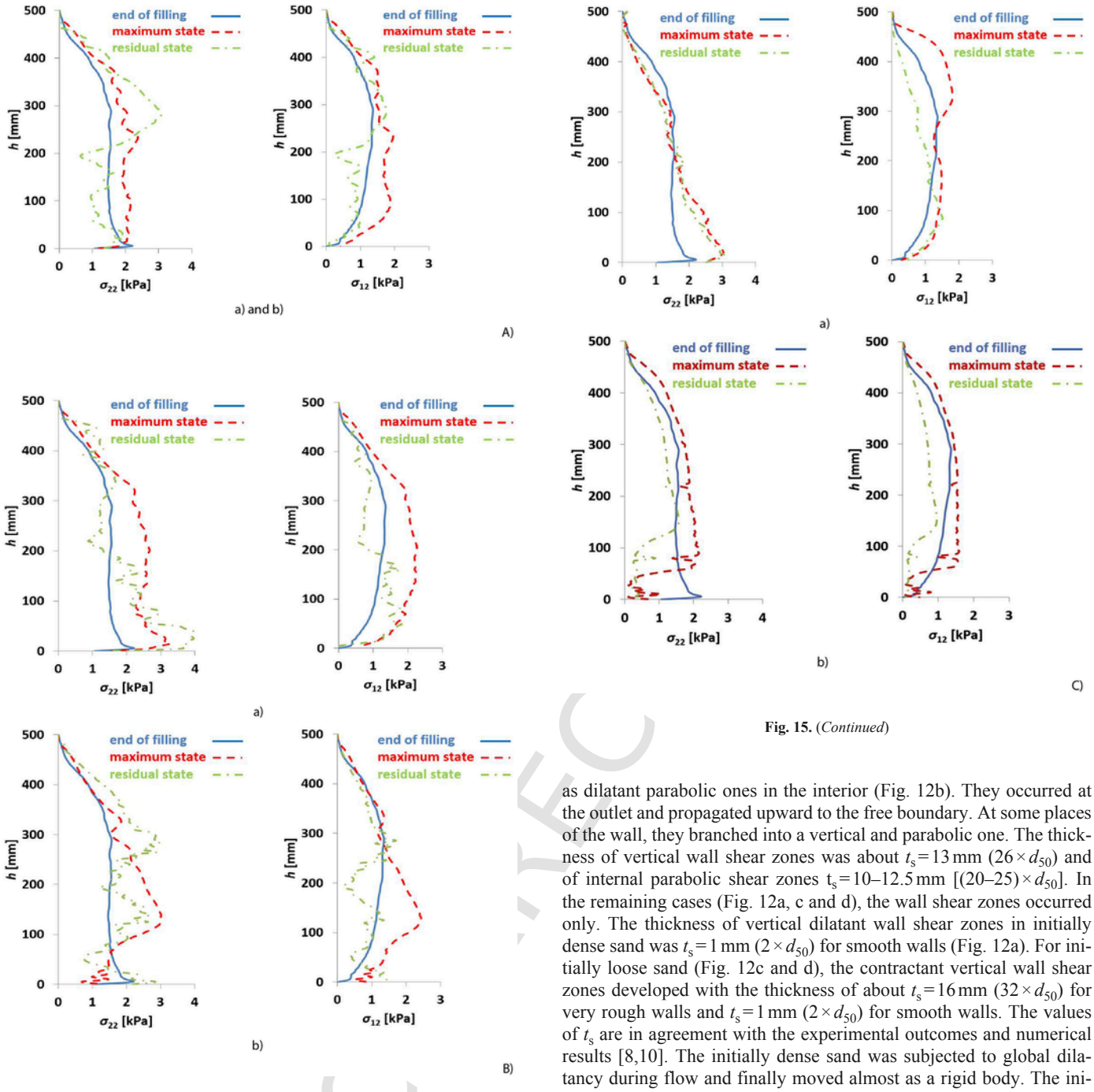

Fig. 15. Calculated distribution of wall stresses (σ_{22} - wall horizontal stress and σ_{12} - wall shear stress) after bottom displacement in model silo with initially dense sand ($e_o = 0.60$) and very rough walls for different width and location of silo outlet: A) symmetric outlet with width of 80 mm, B) asymmetric outlet with width of 150 mm and C) asymmetric outlet with width of 50 mm (a) left wall and b) right wall) ('maximum state' corresponds to maximum resultant wall normal force N_{max} and 'residual state' corresponds to residual wall friction angle $\varphi_{w,res}$).

ment and its drop after reaching the maximum was insignificant as in the experiment.

6.2. Evolution of shear zones

Shear zones appeared in moving initially dense sand with very rough walls as vertical dilatant vertical shear zones along walls and

Fig. 15. (*Continued*)

as dilatant parabolic ones in the interior (Fig. 12b). They occurred at the outlet and propagated upward to the free boundary. At some places of the wall, they branched into a vertical and parabolic one. The thickness of vertical wall shear zones was about $t_s = 13$ mm ($26 \times d_{50}$) and of internal parabolic shear zones $t_s = 10$–12.5 mm [$(20$–$25) \times d_{50}$]. In the remaining cases (Fig. 12a, c and d), the wall shear zones occurred only. The thickness of vertical dilatant wall shear zones in initially dense sand was $t_s = 1$ mm ($2 \times d_{50}$) for smooth walls (Fig. 12a). For initially loose sand (Fig. 12c and d), the contractant vertical wall shear zones developed with the thickness of about $t_s = 16$ mm ($32 \times d_{50}$) for very rough walls and $t_s = 1$ mm ($2 \times d_{50}$) for smooth walls. The values of t_s are in agreement with the experimental outcomes and numerical results [8,10]. The initially dense sand was subjected to global dilatancy during flow and finally moved almost as a rigid body. The initially loose sand was first subjected to insignificant loosening and then to continuous low contractancy.

6.3. Evolution of wall pressures (tractions)

The distribution of the wall horizontal stress σ_{22} and wall shear stress σ_{12} was demonstrated for the different initial void ratio of sand along the silo wall of the different roughness. The wall stresses were computed in material points close to the walls. They were calculated after filling for the maximum horizontal wall force N_{max} (described as 'maximum state') and for the residual wall friction angle φ_w^{res} ($u = 20$ mm) (described 'residual state'). The wall tractions significantly changed in initially dense sand with very rough walls after bottom displacement u (Figs. 12b and 13b). They strongly increased and

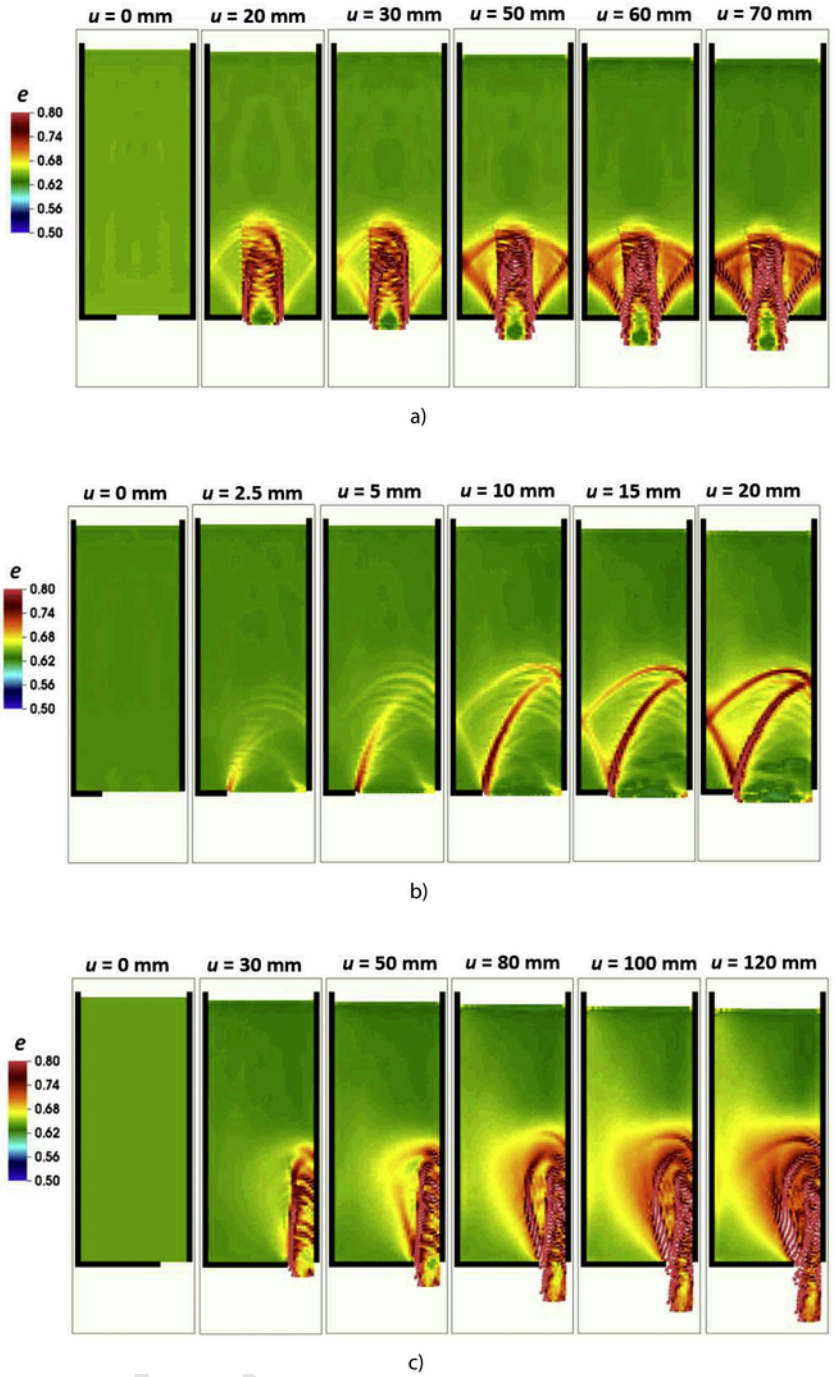

Fig. 16. Calculation evolution of void ratio in initially dense sand ($e_o = 0.60$) after bottom displacement u in model silo with smooth walls for different width and location of outlet: a) symmetric outlet with width of 80 mm, b) asymmetric outlet with width of 150 mm and c) asymmetric outlet with width of 50 mm.

then gradually decreased until a residual state was obtained. They also oscillated with wandering peaks due to the presence of internal curvilinear shear zones [10]. Thus, a strongly non-regular distribution of wall stresses along the wall was obtained (Fig. 13b). In the remaining cases, the distribution of wall pressures only slightly changed after bottom displacement and their oscillations were negligible (Fig. 13a, c and d). The highest wall horizontal stress was obviously for smooth walls independently of the initial void ratio ($\sigma_{22(max)} = 4$–4.5 kPa) (Fig. 13a and c). For very rough walls, the maximum horizontal stress was $\sigma_{22(max)} = 2.6$ kPa. The wall distribution of σ_{22} during flow was almost linear for smooth walls. The highest wall shear stress σ_{12} was obviously for very rough walls with initially dense sand $\sigma_{12(max)} = 2.4$ kPa (Fig. 13b) while $\sigma_{12(max)} = 1.0$ kPa for smooth walls (Fig. 13a and c).

7. Quasi-static sand flow with controlled outflow for different outlet width and location

Figs. 14–21 demonstrate the effect of the different both outlet width and location on shear localization and wall stresses in initially

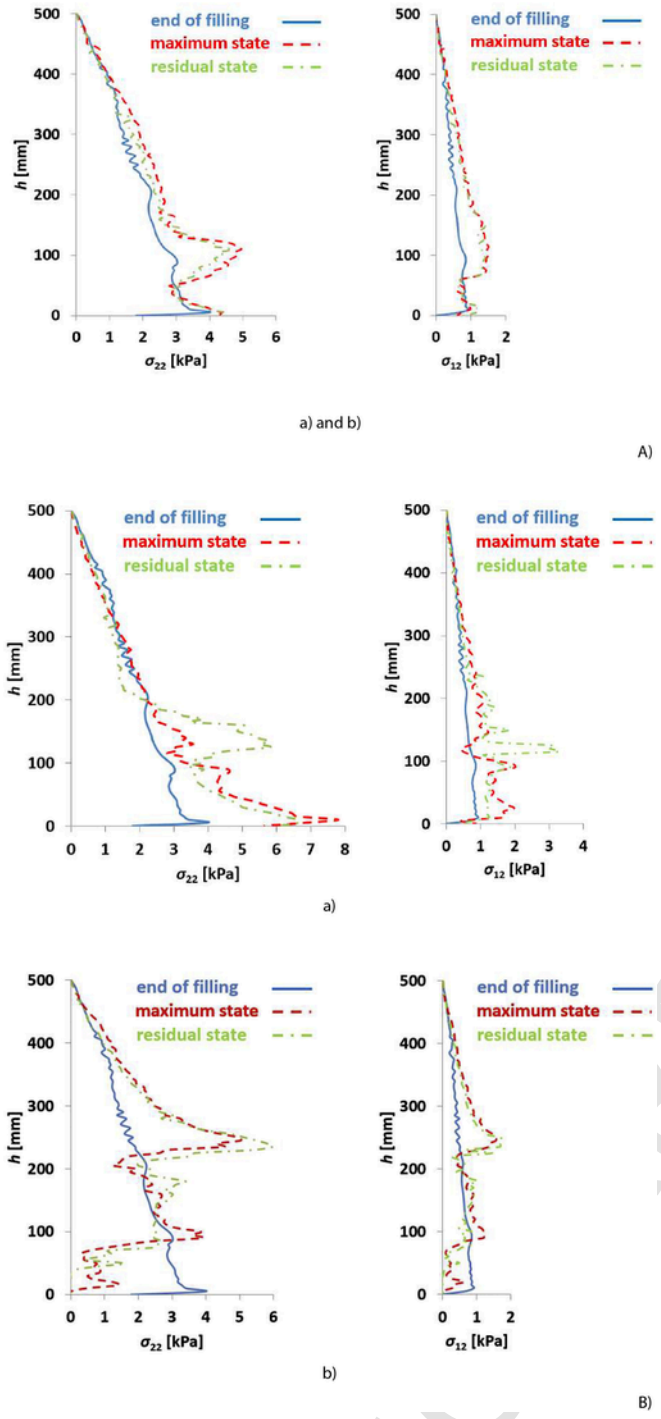

Fig. 17. Calculated distribution of wall stresses (σ_{22} - wall horizontal stress and σ_{12} - wall shear stress) after bottom displacement in model silo with initially dense sand ($e_o = 0.60$) and smooth walls for different width and location of silo outlet: A) symmetric outlet with width of 80 mm, B) asymmetric outlet with width of 150 mm and C) asymmetric outlet with width of 50 mm (a) left wall and b) right wall) ('maximum state' corresponds to maximum resultant wall normal force N_{max} and 'residual state' corresponds to residual wall friction angle $\varphi_{w,res}$).

dense/loose sand with very rough/smooth walls during quasi-static flow of sand mass with a constant outlet velocity prescribed along the movable bottom of a smaller width than the width of the model silo of Section 6 ($b = 0.20$ m). The outlet was either symmetrically (case '1') or asymmetrically located (case '2') with respect to a vertical

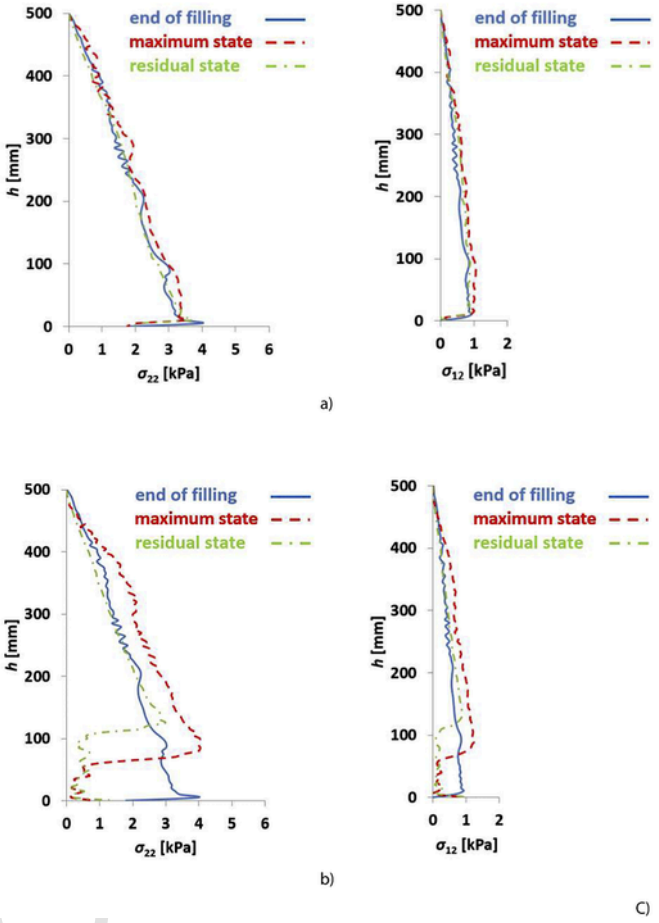

Fig. 17. (*Continued*)

symmetric line. It the case '1', the outlet width was $b = 80$ mm (Fig. 14a) and in the case '2', the outlet width was $b = 150$ mm (Fig. 14b) or $b = 50$ mm (Fig. 14c). The results with initially dense sand ($e_o = 0.60$) at very rough walls are demonstrated in Figs. 14 and 15, the results with initially dense sand ($e_o = 0.60$) at smooth walls are in Figs. 16 and 17, the results with initially loose sand ($e_o = 0.90$) at very rough walls are in Figs. 18 and 19. Finally, Figs. 20 and 21 show the results with initially loose sand ($e_o = 0.90$) at smooth walls. All initial and boundary conditions and the time increment were the same as in Section 6.

7.1. Evolution of shear zones

The width and location of the silo outlet, and wall roughness and initial void ratio strongly affected the flow pattern of sand and pattern of internal shear zones in sand during emptying. In almost all cases, funnel flow took place. The mass flow in the silo (beyond the outlet region) was mainly preserved in initially loose sand (Figs. 18, and 20). The pattern of internal curvilinear shear zones in the model silo with very rough walls and initially dense sand during asymmetric flow (Fig. 14b and c) was more complex than during symmetric mass flow ($b = 200$ mm) (Fig. 12b). It was also affected by the close location of a rigid wall at the outlet. If the outlet was located at the wall, the phenomenon of multiply branching of shear zones occurred in initially dense sand both at very rough walls (Fig. 14b and c) and smooth walls (Fig. 16b and c). For the smaller symmetric/asymmetric outlet widths with very rough/smooth walls of $b = 80$ mm (Figs. 14a

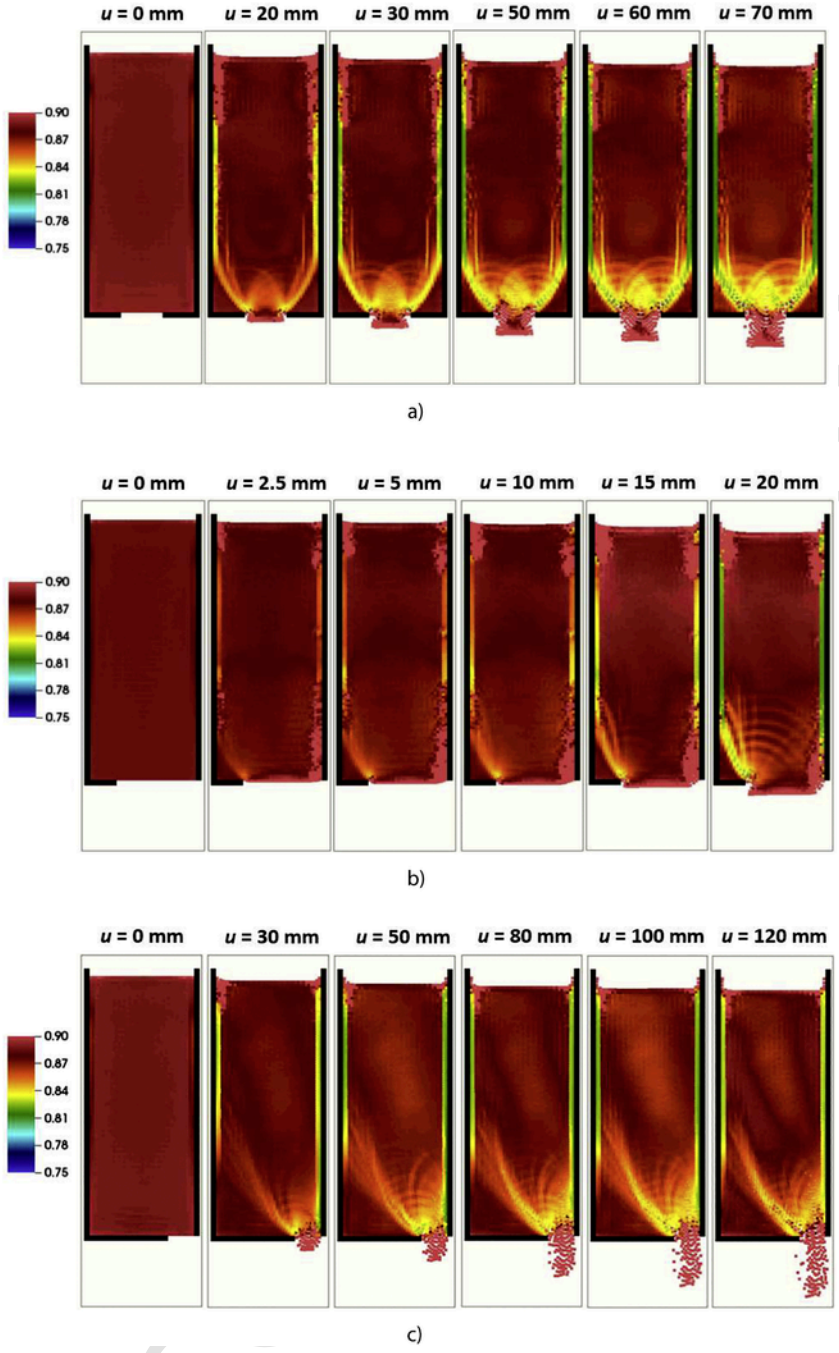

Fig. 18. Calculation evolution of void ratio in initially loose sand ($e_o = 0.90$) after bottom displacement u in model silo with very rough walls for different width and location of outlet: a) symmetric outlet with width of 80 mm, b) asymmetric outlet with width of 150 mm and c) asymmetric outlet with width of 50 mm.

and 16a) and $b = 50$ mm (Figs. 14c and 16c), a large dilatant region occurred above the outlet. All wall and internal shear zones in initially loose sand were subjected to contractancy (Figs. 18 and 20). For initially loose sand, a pattern of internal curvilinear shear zones was mainly limited to the small region above the outlet (Figs. 18 and 20). The number of internal shear zone was also higher with very rough walls. The contractant shear zones (Figs. 18 and 20) were more flat than the dilatant ones (Figs. 14 and 16).

7.2. Evolution wall pressures

The evolution of wall stresses was also affected by a flow pattern in moving sand. For the symmetric flow of initially dense sand ($e_o = 0.60$) in the silo model with very rough walls (Fig. 15A), initially the horizontal and shear wall stresses slightly increased in the first emptying phase, as compared to the filling state. Next, the mixed flow appeared and the wall stresses significantly increased above the effective transition point between funnel and mass flow and decreased below this point. The maximum wall stresses in the lower

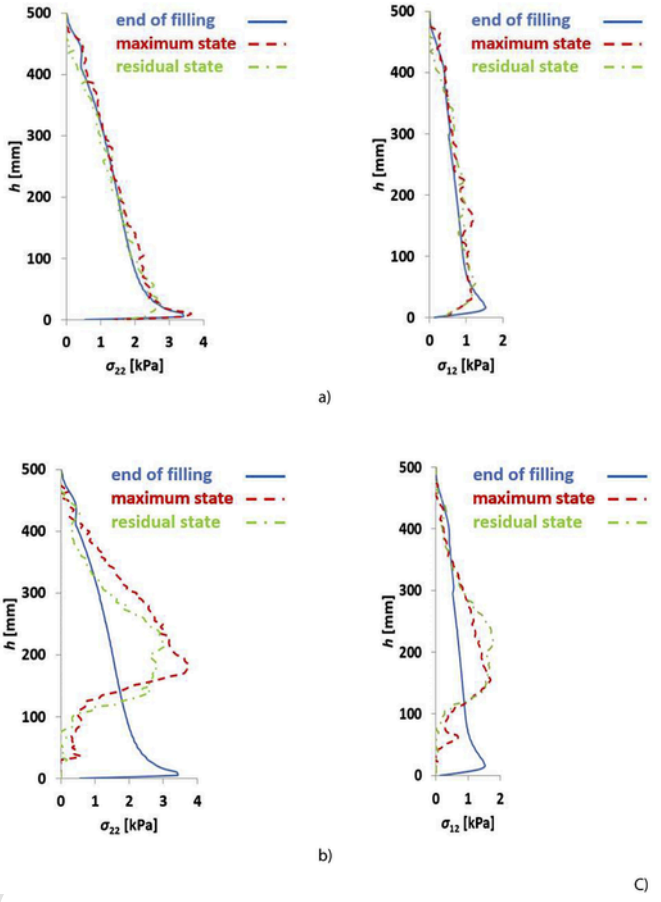

Fig. 19. (*Continued*)

Fig. 19. Calculated distribution of wall stresses (σ_{22} - wall horizontal stress and σ_{12} - wall shear stress) after bottom displacement in model silo with initially loose sand ($e_o = 0.90$) and very rough walls for different width and location of silo outlet: A) symmetric outlet with width of 80 mm, B) asymmetric outlet with width of 150 mm and C) asymmetric outlet with width of 50 mm (a) left wall and b) right wall) ('maximum state' corresponds to maximum resultant wall normal force N_{max} and 'residual state' corresponds to residual wall friction angle $\varphi_{w,res}$).

silo region after bottom displacement ($\sigma_{22(max)} = 2.2$ kPa and $\sigma_{12(max)} = 2.0$ kPa) were smaller by about 15–20% than for the symmetric flow with $b = 200$ mm (Fig. 13b) except for the upper region at the residual state where the larger wall horizontal wall stresses ($\sigma_{22(max)} = 3.0$ kPa) happened. The wall stresses strongly oscillated.

For the slightly asymmetric outlet with very rough walls and the outlet width of $b = 150$ mm (Fig. 15B), the maximum wall horizontal stresses after bottom displacement were higher along the opposite (left) wall than along the right wall at which the flow took place ($\sigma_{22(max)} = 4.0$ kPa versus $\sigma_{22(max)} = 3.0$ kPa). Thus, they were higher for $b = 150$ mm by 15%–50% than for $b = 200$ mm ($\sigma_{22(max)} = 2.6$ kPa) (Fig. 13b). The maximum wall shear stresses were similar along both the vertical walls ($\sigma_{12(max)} = 2.3$–2.4 kPa) and also similar to the silo width $b = 200$ mm ($\sigma_{12(max)} = 2.4$ kPa) (Fig. 13b). When the outlet of the smaller width of $b = 50$ mm was strongly asymmetric (Fig. 15C), the maximum wall horizontal stresses after bottom displacement were again higher along the left wall than along the right wall ($\sigma_{22(max)} = 3.0$ kPa versus $\sigma_{22(max)} = 2.3$ kPa). They were respectively higher/smaller by 15%/10% than for $b = 200$ mm (Fig. 15b). The maximum wall shear stresses were similar for both the walls ($\sigma_{12(max)} = 1.7$–1.8 kPa) and were lower by 25% than for $b = 200$ mm (Fig. 13b). The wall stresses strongly reduced in the lower silo part at the right wall during emptying due to pronounced material loosening.

For smooth walls and initially dense sand ($e_o = 0.60$) (Fig. 17), the horizontal wall stresses were obviously higher and the shear wall stresses were smaller than for very rough walls (Fig. 17). With a symmetric outlet ($b = 80$ mm), a symmetric funnel flow initially occurred that caused an increase of wall stresses at the effective transition level between mass and funnel flow (Fig. 17A). For a large asymmetric outlet ($b = 150$ mm) (Fig. 17B), the asymmetric funnel flow took place that resulted in asymmetric wall stress distribution, i.e. a signif-

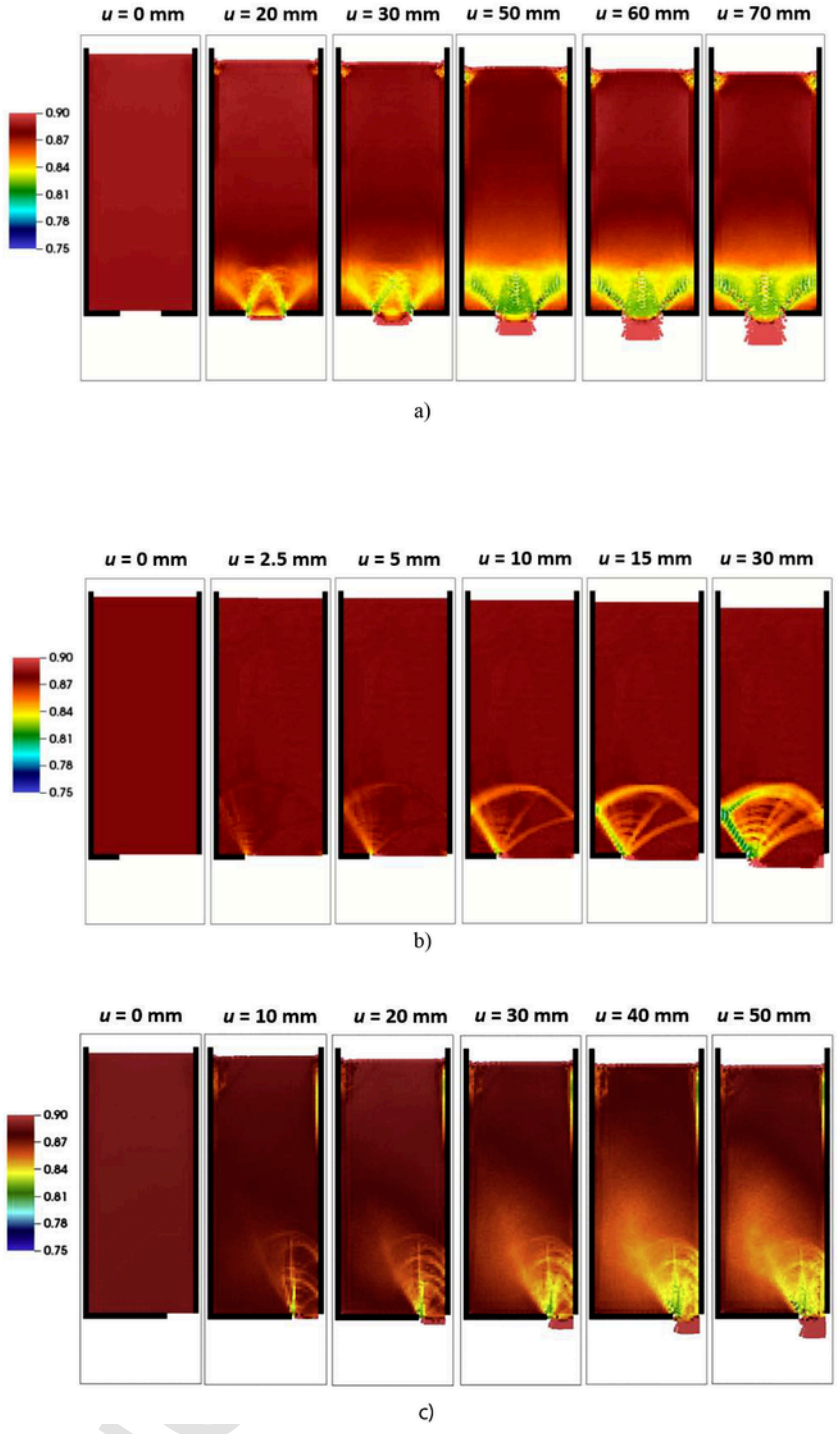

Fig. 20. Calculation evolution of void ratio in initially loose sand ($e_o = 0.90$) after bottom displacement u in model silo with smooth walls for different width and location of silo outlet: a) symmetric outlet with width of 80 mm, b) asymmetric outlet with width of 150 mm and c) asymmetric outlet with width of 50 mm.

icant increase in the lower part of the opposite (left) wall and a pronounced increase above the effective transition and a decrease below it on the right wall at which the flow took place. For a small asymmetric opening ($b = 50$ mm) (Fig. 17C), due to the material dead region along the left side wall, the wall stresses on the right side of the silo solely changed, i.e. the wall stresses slightly increased (less than for $b = 150$ mm) except for the lower wall part where they strongly dropped.

For very rough walls and initially loose sand ($e_o = 0.90$) (Fig. 19), the increase of wall stresses after bottom displacement was smaller due to small contractant volume changes as compared to initially dense sand with high dilatant volume changes. As usually, the wall stresses increased above the effective transition point between mass and funnel flow and diminished below it with a symmetric outlet (b = 50 mm) (Fig. 19A). With non-symmetric outlets (Fig.19B and C), the maximum horizontal wall stresses were in contrast to initially

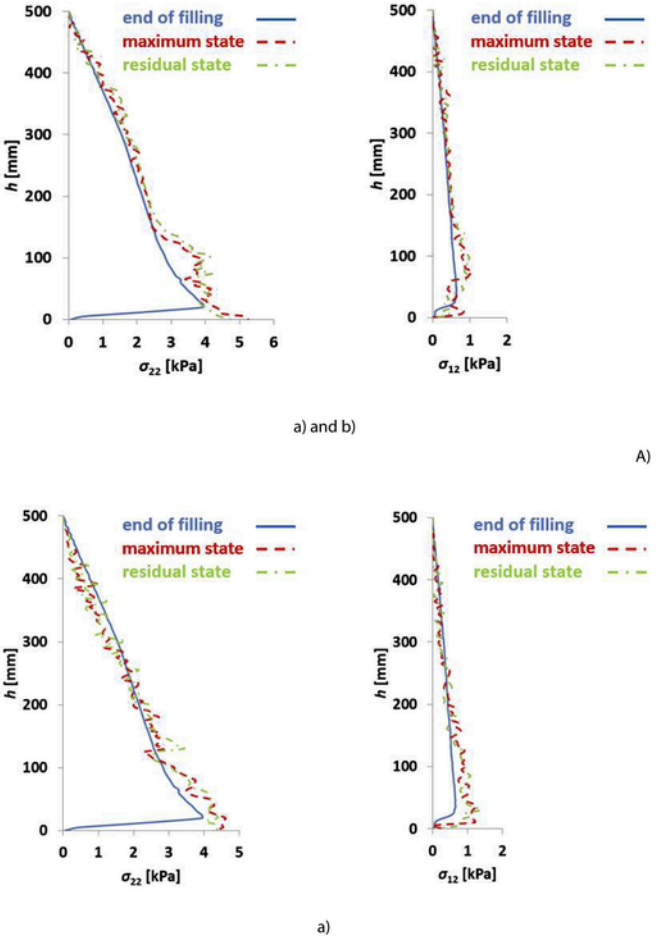

Fig. 21. Calculated distribution of wall stresses (σ_{22} - wall horizontal stress and σ_{12} - wall shear stress) after bottom displacement in model silo with initially loose sand ($e_o = 0.90$) and smooth walls for different width and location of silo outlet: A) symmetric outlet with width of 80 mm, B) asymmetric outlet with width of 150 mm and C) asymmetric outlet with width of 50 mm (a) left wall and b) right wall) ('maximum state' corresponds to maximum resultant wall normal force N_{max} and 'residual state' corresponds to residual wall friction angle $\varphi_{w,res}$).

dense sand higher at the right wall at which the flow took place. The behaviour of wall stresses on the right side was similar in all cases. On the left side, the wall stresses insignificantly changed during flow.

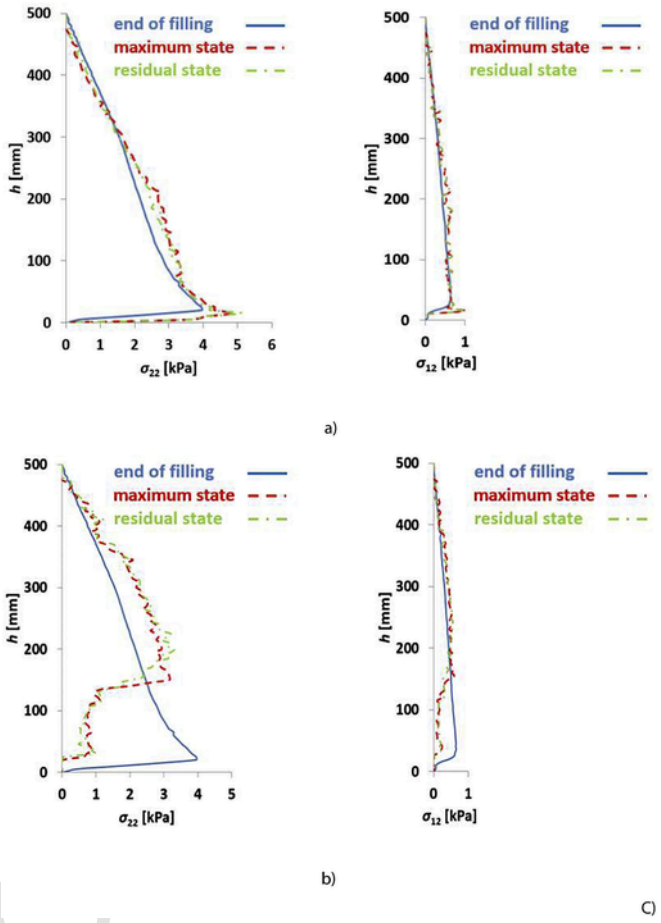

Fig. 21. (*Continued*)

The behaviour of initially loose sand with smooth walls was similar (Fig. 21). The increases of wall stresses were still slightly lower than in Fig. 19.

In general, for asymmetric outlets, the horizontal wall stresses in the lower part of the silo increased after bottom displacement at the opposite wall (at which flow did not take place) and decreased at the wall at which flow took place. A similar conclusion was derived in [90]. The outcome is different that this given in the silo Eurocode 1 [89] for large silo discharge eccentricities wherein the increase of horizontal pressures at the opposite wall is not expected.

The flow behaviour of granular materials is always affected by a size effect caused mainly by the different both the pressure level and ratio between the silo diameter/width and mean grain size of the solid [8,14,91,92]. Thus, the nominal wall stresses in silos always become higher with reducing silo size since both mobilized friction and dilatancy of bulk solids increase with reducing pressure. Similarly, the nominal wall stresses reduce when the ratio between the mean grain diameter and silo diameter/width decreases since the width of shear zones is related to the mean grain diameter.

Finally, to show the capability of the MPM method for simulating dynamic emptying in silos due to gravity, some calculations were also performed for the silo model with initially dense sand ($e_o = 0.60$) and very rough walls assuming a symmetric narrow outlet ($b = 80$ mm) (Fig. 22). The hypoplastic constitutive model was extended by the intergranular strain to avoid a ratcheting phenomenon [60] (its effect was, however, insignificant on the flow pattern). The dynamic viscosity was neglected [61]. The numerical results regard-

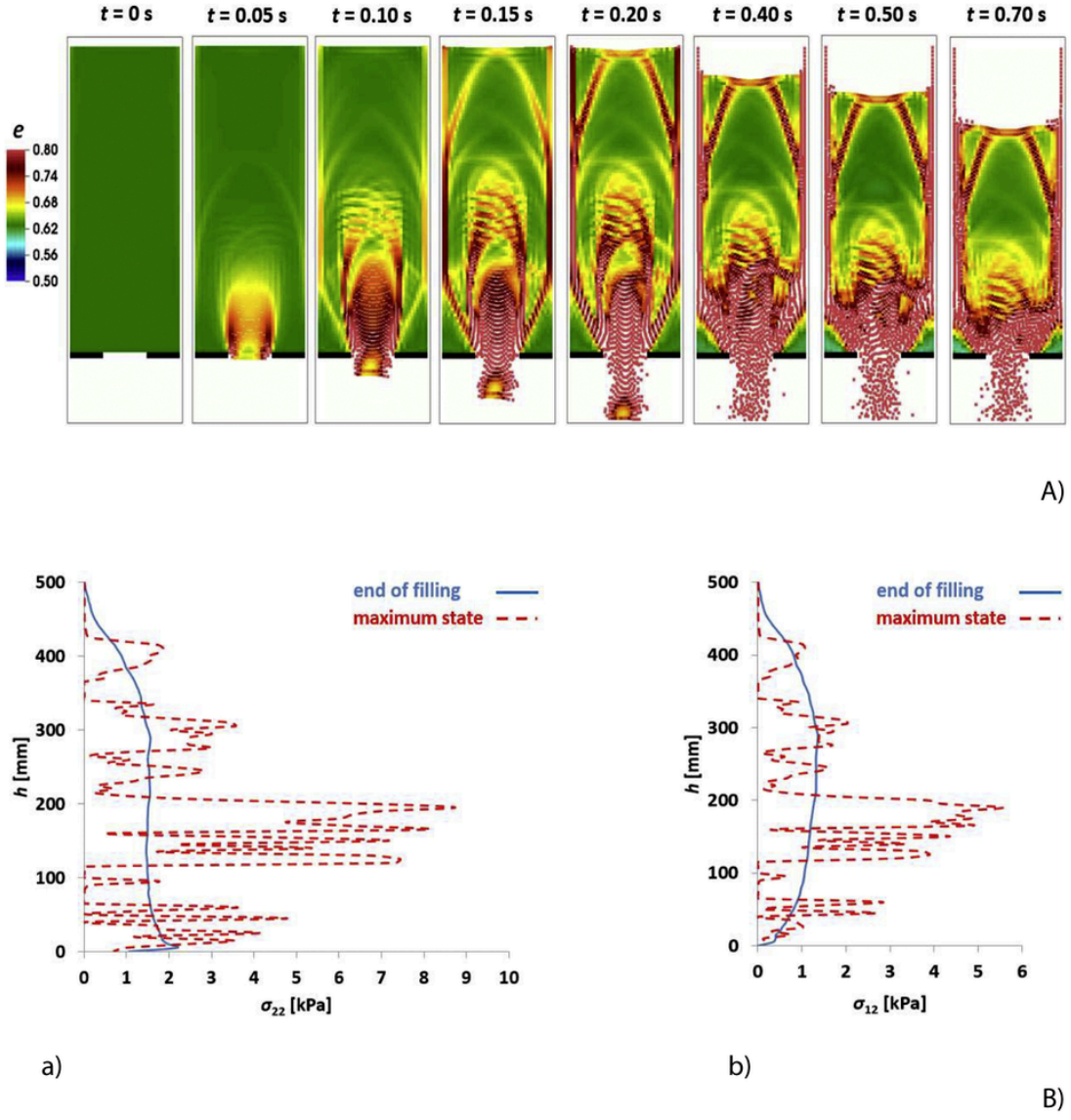

Fig. 22. Numerical results dynamic gravitational granular outflow in model silo with very rough walls, initially dense sand (e_o=0.60) and symmetric outlet with width of 80 mm: A) evolution of void ratio during flow and B) distribution of wall stresses (σ_{22} - wall horizontal stress (a) and σ_{12} - wall shear stress (b), 'maximum state' corresponds to maximum resultant wall normal force).

ing the flow pattern and wall stresses are demonstrated in Fig. 22A and B.

As compared to quasi-static flow (Fig. 14a), the dynamic flow pattern of sand was similar (Fig. 22A). However, a slightly wider and higher funnel flow was created above the silo outlet during dynamic emptying. The material in a funnel flow region was looser. In addition, more internal shear zones occurred. The effective transition point was also located at a lower height above the outlet. The wall stresses during dynamic flow (Fig. 22B) were more non-uniform than those during quasi-static flow (Fig. 15A) [8]. The peak dynamic wall stresses values were locally higher by about 3 times than for quasi-static flow. The dynamic silo flow merits further numerical investigations.

8. Conclusions

The results of a series of MPM simulations of quasi-static cohesionless sand flow in a silo model with parallel walls and controlled outlet velocity were presented by taking shear localization into account. In the simulations, the initial void ratio of sand, wall roughness, outlet width and outlet location were varied. Comparisons of results between the MPM simulations and physical silo tests showed good agreement in measured resultant wall and bottom forces, wall friction angles and thickness of wall shear zones. Some main conclusions may be drawn from our calculations:

- The MPM approach allowed for simulating bulk solid flow without excessive mesh distortion. The numerical outcomes were insensitive to the number of material points and a time increment. It produced trends consistent with those observed in the physical experiments. It realistically captured shear localization in the form of both the vertical wall and internal curvilinear shear zones.
- The initial void ratio of the solid and the silo wall roughness were found both to have a huge influence on the resultant wall and bottom forces, the thickness of wall shear zones and the pattern of internal curvilinear shear zones.
- The magnitudes of wall stresses/forces were strictly combined with the thickness of wall shear zones that increased with both growing wall roughness and initial void ratio. The wall stresses during emptying were strongly affected by those during the filling state. The wall shear zone was dilatant in initially dense sand and contractant in initially loose sand. It is of great importance to properly model the thickness of wall shear zones for realistic evaluation of wall stresses/forces.
- The pattern of both granular flow and internal curvilinear shear zones was affected by the location and width of the outlet, wall roughness and initial void ratio of sand. The internal curvilinear shear zone always occurred during the asymmetric flow independently of the wall roughness and initial void ratio and during mass flow in initially dense sand with very rough walls. The pattern was very complex during asymmetric flow of initially dense sand at the wall.
- The internal shear zones had a tendency to multiply branching at several points along the wall. The curvature of internal shear zones increased with a diminishing initial void ratio of sand. The internal shear zones caused both the oscillation and non-uniform distribution of wall pressures in particular for very rough walls and initially dense sand. Thus, it is also of great importance to properly model the thickness and shape of internal shear zones for realistic evaluation of wall stresses.
- The maximum horizontal wall stresses happened for smooth walls and the maximum shear wall stresses occurred in initially dense sand with very rough walls. In general, the smaller outlet width decreased the wall pressures during symmetric flow. The significant wall stresses growths appeared at the effective transition between mass and funnel flow. Below the transition level, the wall stresses decreased. The asymmetric outlets either increased more the horizontal wall stress on the opposite wall at which flow did not take place (initially dense sand) or increased more the horizontal wall stress on the wall at which flow occurred (initially loose sand).

CRediT authorship contribution statement

J. Krzyżanowski: Methodology, Software, Investigation, Formal analysis, Visualization, Writing - original draft. **J. Tejchman:** Conceptualization, Writing - original draft, Validation, Supervision, Funding acquisition. **W. Sołowski:** Software, Writing - review & editing. **M. Wójcik:** Conceptualization, Investigation, Supervision, Writing - review & editing.

Declaration of Competing Interest

None.

Acknowledgements

The research work has been carried out within the project "*Autogeneous coupled dynamic-acoustic effects in granular materials - experiments and coupled DEM/CFD approach*" financed by the National Science Centre, Poland (UMO-2017/27/B/ST8/02306).

Appendix A. Appendix

The local hypoplastic model [16] describes the evolution of normalized stress tensor $\hat{\boldsymbol{T}}_{\mathrm{s}}$ with the evolution of rate of deformation tensor $\boldsymbol{D}_{\mathrm{s}}$ using isotropic linear and non-linear tensorial functions, $\boldsymbol{L}$ and $\boldsymbol{N}$.

$$\dot{e} \tag{A1}$$

with

$$\hat{\boldsymbol{T}}_{\mathrm{s}} = \frac{\boldsymbol{T}_{\mathrm{s}}}{tr\boldsymbol{T}_{\mathrm{s}}} \tag{A2}$$

where $\overset{\circ}{\boldsymbol{T}}_{\mathrm{s}}$ - the Jaumann stress rate tensor, f_{s} - the stiffness factor, f_{d} - the density factor, $\hat{\boldsymbol{T}}_{\mathrm{s}}$ - the normalized granular stress tensor and $\boldsymbol{T}_{\mathrm{s}}$ - the Cauchy stress tensor (index 's' denotes the skeleton). The following representations for $\boldsymbol{L}$ and $\boldsymbol{N}$ (which are linear and nonlinear in respect to deformation tensor $\boldsymbol{D}_{\mathrm{s}}$) are proposed

$$\dot{e} \tag{A3}$$

$$\boldsymbol{N}\left(\hat{\boldsymbol{T}}_{\mathrm{s}}\right) = a_1\left(\hat{\boldsymbol{T}}_{\mathrm{s}} + \hat{\boldsymbol{T}}_{\mathrm{s}}^{*}\right) \tag{A4}$$

where

$$\begin{aligned} a_1^{-1} &= c_1 + c_2\left\|\hat{\boldsymbol{T}}_{s}^{*}\right\|\left[1+\cos(3\theta)\right] \; and \; \cos(3\theta) \\ &= -\sqrt{6}\frac{tr\left(\hat{\boldsymbol{T}}_{\mathrm{s}}^{*3}\right)}{\left[tr\left(\hat{\boldsymbol{T}}_{\mathrm{s}}^{2}\right)\right]^{1.5}} \end{aligned} \tag{A5}$$

$$c_1 = \sqrt{\frac{3}{8}}\frac{\left(3-\sin\varphi_{\mathrm{c}}\right)}{\sin\varphi_{\mathrm{c}}} \; and \; c_2 = \frac{3}{8}\frac{\left(3+\sin\varphi_{\mathrm{c}}\right)}{\sin\varphi_{\mathrm{c}}} \tag{A6}$$

$$\hat{\boldsymbol{T}}_{\mathrm{s}}^{*} = \hat{\boldsymbol{T}}_{\mathrm{s}} - \frac{1}{3}\boldsymbol{I} \tag{A7}$$

with φ_{c} – the critical angle of internal friction during stationary flow, θ - the Lode angle and $\hat{\boldsymbol{T}}_{\mathrm{s}}^{*}$ - the deviatoric part of normalized stress tensor $\hat{\boldsymbol{T}}_{\mathrm{s}}$. The influence of the current void ratio and pressure level is taken into account by the stiffness factor f_{s} (proportional to the granular hardness h_{s} and depending also on the mean stress and void ratio) and the density factor f_{d} which are represented as.

$$
\begin{aligned}
f_s &= f_b f_e \\
&= \frac{h_s}{n h_i}\left(\frac{e_i}{e}\right)^{\beta}\frac{1+e_i}{e_i}\left(\frac{3p_s}{h_s}\right)^{1-n} \text{ and } f_d \\
&= \left(\frac{e-e_d}{e_c-e_d}\right)^{\alpha}
\end{aligned}
\tag{A8}
$$

where α - the pycnotropy coefficient, n – the compression coefficient, β – the stiffness coefficient, a_1 - the parameter representing the deviatoric part of the normalized stress in critical states, e_c - the critical void ratio, e_d - the void ratio at maximum densification and e_i - the maximum void ratio. The current void ratio e is updated during calculations by the formula

$$
\dot{e} = (1+e)\, tr\boldsymbol{D}_s \tag{A9}
$$

where $\dot{e}$ – the rate of void ratio (e is limited by e_i and e_d). The values of e_i, e_d and e_c decrease with the pressure p_s according to the exponential functions:

$$
\begin{aligned}
e_i &= e_{i0} \bullet \exp\left[-\left(\frac{-3p_s}{h_s}\right)^n\right], e_d \\
&= e_{d0} \bullet \exp\left[-\left(\frac{-3p_s}{h_s}\right)^n\right], e_c \\
&= e_{c0} \bullet \exp\left[-\left(\frac{-3p_s}{h_s}\right)^n\right]
\end{aligned}
\tag{A10}
$$

where $e_{i0,}$ $e_{d0,}$ e_{c0} are the values of e_i, e_d and e_c for the granular pressure $p_s = 0$.

References

[1] A.W. Jenike, Storage and flow bulk of solids, Eng. Exp. Station. Bull (1964), No 123, University Utah.

[2] J. Schwedes, Fließverhalten von Schüttgütern in Bunkern, Wein-heim/ Bergstraße, Verlag Chemie, 1970.

[3] N. Fayed, L. Otten, Handbook of Powder Science and Technology, Chapmann and Hall, 1984.

[4] S.S. Safarian, E.C. Harris, Design and Construction of Silos and Bunkers, Van Nostrand Reinhold Company, 1985.

[5] J. Ravenet, Silo problems, Bulk Solids Handling 1 (4) (1981) 667–679.

[6] J.W. Carson, In: Silo Failures: Case Histories and Lessons Learned, Proc. 3rd Israeli Conf. for Conveying and Handling of Particulate Solids, Dead Sea, Israel, 1, 2000, pp. 1–4.

[7] A. Dogangun, Z. Karaca, A. Durmus, M. Halil Sezen, Cause of damage and failures in silo structures, J. Perform. Constr. Facil. ASCE 23 (2) (2009) 65–71.

[8] J. Tejchman, Confined Granular Flow in Silos – Experiments and Numerical Investigations, Springer, Berlin-Heidelberg, 2013.

[9] K. Wilde, J. Tejchman, M. Rucka, M. Niedostatkiewicz, Experimental and theoretical investigations of silo music, Powder Technol. 198 (1) (2010) 38–48.

[10] M. Wójcik, J. Tejchman, Modeling of shear zone localization during confined granular flow in silos with non-local hypoplasticity, Powder Technol. 192 (2009) 298–310.

[11] M. Wójcik, M. Sondej, K. Rejowski, J. Tejchman, Full-scale experiments on wheat flow in steel silo composed of corrugated walls and columns, Powder Technol. 311 (2017) 537–555.

[12] M. Wójcik, J. Härtl, J.Y. Ooi, J.M. Rotter, S. Ding, G.G. Enstad, Experimental investigation of flow pattern and wall pressure distribution in a silo with double-cone insert, Part. Part. Syst. Charact. 24 (4–5) (2007) 296–303.

[13] M. Niedostatkiewicz, M. Wójcik, J. Tejchman, Application of inserts for suppression of coupled dynamic-acoustic effects during confined granular flow in silos, Adv. Powder Technol. 25 (1) (2014) 398–407.

[14] J. Tejchman, FE Modeling of Shear Localization in Granular Bodies with Micro-Polar Hypoplasticity, Springer Series in Geomechanics and Geoengineering, Berlin-Heidelberg, 2008.

[15] G. Gudehus, A comprehensive constitutive equation for granular materials, Soils Found 36 (1) (1996) 1–12.

[16] E. Bauer, Calibration of a comprehensive hypoplastic model for granular materials, Soils Found 36 (1) (1996) 13–26.

[17] P.A. von Wolffersdorff, A hypoplastic relation for granular materials with a predefined limit state surface, Mech. Cohes. Frict. Mater. 1 (1996) 251–271.

[18] J. Tejchman, Influence of a characteristic length on shear zone formation in hypoplasticity with different enhancements, Comput. Geotech. 31 (8) (2004) 595–611.

[19] D. Sulsky, S.J. Zhou, H.L. Schreyer, Application of a particle-in-cell method to solid mechanics, Comput. Phys. Commun. 87 (1995) 236–252.

[20] Z. Chen, R. Brannon, An Evaluation of the Material Point Method, SAND Report, Sandia National Laboratories Albuquerque, New Mexico and Livermore, California, 2002.

[21] Z. Wieckowski, The material point method in large strain engineering problems, Comput. Methods Appl. Mech. Eng. 193 (39–411) (2004) 4417–4438.

[22] L. Beuth, Z. Wieckowski, P.A. Vermeer, Solution of quasi-static large-strain problems by the material point method, Int. J. Num. Anal. Meths. Geom. 35 (1313) (2011) 1451–1465.

[23] W.T. Sołowski, S.W. Sloan, Evaluation of material point method for use in geotechnics, Int. J. Numer. Anal. Methods Geomech. 39 (2015) 685–701.

[24] P. Hajko, J. Tejchman, Modelling of shear localization during granular flow within non-local hypoplasticity using material point method, in: W. Wu (Ed.), Bifurcation and Degradation of Geomaterials with Engineering Applications, Springer Series in Geomechanics and Geoenginering, Proc. 11th Int. Workshop on Bifurcation and Degradation in Geomechanics, Limassol, Cyprus, 21–25.05, 2017, pp. 593–599.

[25] Uintah Software, Utah University (USA), in: http://www.uintah.utah.edu/.

[26] I. Vardoulakis, Shear band inclination and shear modulus in biaxial tests, Int. J. Numer. Anal. Methods Geomech. 4 (1980) 103–119.

[27] J. Tejchman, Scherzonenbildung und Verspannungseffekte in Granulaten unter Berücksichtigung von Korndrehungen, 117, Publication Series of the Institute of Soil and Rock Mechanics, University Karlsruhe, 1989.

[28] Hibbitt Abaqus, User's manual, version 6.4, Karlsson & Sorensen, Inc., 2004.

[29] N. Phuong, A. van Tol, A. Elkadi, A. Rohe, Modelling of pile installation using the material point method (MPM), Numer. Methods Geotech. Eng. 271 (2014).

[30] T. Bhandari, F. Hamad, C. Moormann, K.G. Sharma, B. Westrich, Numerical modelling of seismic slope failure using MPM, Comput. Geotech. 75 (2016) 126–134.

[31] F. Ceccato, I. Redaelli, C. di Prisco, P. Simonini, Impact forces of granular flows on rigid structures: comparison between discontinuous (DEM) and continuous (MPM) numerical approaches, Comput. Geotech. 103 (2018) 201–217.

[32] P.J. Vardon, B. Wang, M.A. Hicks, Slope failure simulations with MPM, J. Hydrodyn. Ser. B 29 (3) (2017) 445–451.

[33] L. Wanga, W.M. Coombs, C.E. Augarde, M. Brown, J. Knappett, A. Brennan, D. Richards, A. Blakec, Modelling screwpile installation using the MPM, Proc. Eng. 175 (2017) 124–132.

[34] Z. Wieckowski, S.-K. Youn, J.H. Yeon, A particle-in-cell solution to the silo discharging problem, Int. J. Num. Meths. Eng. 45 (1999) 1203–1225.

[35] Z. Wieckowski, A material point method in large strain engineering problems, Proc. Eur. Conf. on Comput. Mech. ECCM 99 (1999).

[36] Z. Wieckowski, The material point method in large strain engineering problems, Comput. Methods Appl. Mech. Eng. 193 (2004) 4417–4438.

[37] H.-B. Mühlhaus, H. Sakaguchi, L. Moresi, M. Fahey, Discrete and continuum modelling of granular materials, in: P.A. Vermeer, S. Diebels, W. Ehlers, H.J. Herrmann, S. Luding, E. Ramm (Eds.), Continuous and Discontinuous Modelling of Cohesive-Frictional Materials, Springer, Berlin, 2001, pp. 185–204.

[38] L. Oger, S.B. Savage, M. Sayed, In: Granular Flow using Particle-In-Cell Approach, Proceedings of 4th Euromech Conference, Metz, 1, 2000, p. 126.

[39] Z. Wieckowski, The material point method in the analysis of the problem of shear bounds formation, Comput. Fluid Solid Mech. (2003) 2173–2177.

[40] U. Häußler, J. Eibl, Numerical investigation of discharging silos, J. Eng. Mech. 110 (1984), 975–971.

[41] T. Karlsson, M. Klisiński, K. Runesson, Finite element simulations of granular flow in plane silos with complicated geometry, Powder Technol. 99 (1998) 29–39.

[42] S.A. Elaskar, L.A. Godoy, D.D. Gray, J.M. Stiles, A viscoplastic approach to model the flow of granular solids, Int. J. Solids Struct. 37 (2000) (2000) 2185–2214.

[43] J.U. Böhrnsen, H. Antes, M. Ostendorf, J. Schwedes, Silo discharge: measurement and simulation of dynamic behavior in bulk solids, Chem. Eng. Technol. 27 (2004) (2004) 71–76.

[44] T. Tian, J. Su, J. Zhan, S. Geng, X. Liu, Discrete and continuum modeling of granular flow in silo discharge, Particuology 36 (2018) 127–138.

[45] S. Ding, H. Li, J.Y. Ooi, Prediction of flow patterns during silo discharges using a finite element approach and its preliminary experimental verification, Particuology 18 (2015) 42–49.

[46] Y. Yang, J. Ooi, J.M. Rotter, Y. Wang, Numerical analysis of silo behaviour using non-coaxial models, Chem. Eng. Sci. 66 (2011) 1715–1727.

[47] Y. Wang, Y. Lu, J.Y. Ooi, Finite element modelling of wall pressures in a cylindrical silo with conical hopper using an arbitrary Lagrangian–Eulerian formulation, Powder Technol. 257 (2014) 181–190.

[48] M. Mehrafza, Emptying Pressures in Mass Flow Silos, PhD Thesis Karlsruhe University, 20001–280.

[49] J. Tejchman, M. Klisinski, FE-studies on rapid flow of bulk solids in silos, Granul. Matter 3 (4) (2001) 215–231.

[50] M.A. Martınez, I. Alfaro, M. Doblare, Simulation of axisymmetric discharging in metallic silos. Analysis of the induced pressure distribution and comparison with different standards, Eng. Struct. 24 (2002) 1561–1574.

[51] R. Kobyłka, M. Molenda, DEM modelling of silo load asymmetry due to eccentric filling and discharge, Powder Technol. 233 (2013) 65–71.

[52] Y. Zhang, F. Jia, Y. Zeng, Y. Han, Y. Xiao, DEM study in the critical height of flow mechanism transition in a conical silo, Powder Technol. 331 (2018) 98–106.

[53] Y. Han, F. Jia, G. Li, H. Liu, P. Chen, Numerical analysis of flow pattern transition in a conical silo with ellipsoid particles, Adv. Powder Technol. 30 (9) (2019) 1870–1881.

[54] E. Gallego, J.M. Fuentes, J. Wiącek, J.R. Villar, F. Ayuga, DEM analysis of the flow and friction of spherical particles in steel silos with corrugated walls, Powder Technol. 355 (2019) 425–437.

[55] G.W. Baxter, R.P. Behringer, Cellular automata models for the flow of granular materials, Phys. D 51 (1991) 465–471.

[56] J. Kozicki, J. Tejchman, Application of a cellular automaton to simulations of granular flow in silos, Granul. Matter 7 (2005) 45–54.

[57] J. Tejchman, W. Wu, FE-investigations of non-coaxiality and stress-dilatancy rule in dilatant granular bodies within micro-polar hypoplasticity, Int. J. Numer. Anal. Methods Geomech. 33 (1) (2009) 117–142.

[58] W. Wu, A. Niemunis, Failure criterion, flow rule and dissipation function derived from hypoplasticity, Mech. Cohes. Frict. Mater. 1 (1996) 145–163.

[59] I. Herle, G. Gudehus, Determination of parameters of a hypoplastic constitutive model from properties of grain assemblies, Mech. Cohes. Frict. Mater. 4 (5) (1999) 461–486.

[60] A. Niemunis, I. Herle, Hypoplastic model for cohesionless soils with elastic strain range, Mech. Cohes. Frict. Mater. 2 (1997) 279–299.

[61] J. Tejchman, W. Wu, FE-investigation of shear localization in granular bodies under high shear rate, Granul. Matter 11 (2009) 115–128.

[62] R. Brinkgreve, Geomaterial Models and Numerical Analysis of Softening, Dissertation 1-153, Delft University, 1994.

[63] J.E. Guilkey, J.A. Weiss, Implicit time integration for the material point method: quantitative and algorithmic comparisons with the finite element method, Int. J. Numer. Methods Eng. 57 (9) (2003) 1323–1338.

[64] D. Sulsky, A. Kaul, Implicit dynamics in the material-point method, Comput. Methods Appl. Mech. Eng. 193 (12) (2004) 1137–1170.

[65] B. Wang, P.J. Vardon, M.A. Hicks, Z. Chen, Development of an implicit material point method for geotechnical applications, Comput. Geotech. 71 (2016) 159–167.

[66] M. Goodarzia, M. Rouainiaa, Modelling slope failure using a quasi-static MPM with a non-local strain softening approach, Proc. Eng. 175 (2017) 220–225.

[67] S. Kularathnaa, K. Soga, Implicit formulation of material point method for analysis of incompressible materials, Comput. Methods Appl. Mech. Eng. 313 (2017) 673–686.

[68] I. Iaconetaa, A. Laresea, R. Rossia, E. Onate, An implicit material point method applied to granular flows, Proc. Eng. 175 (2017) 226–232.

[69] S. Bardenhagen, E. Kober, The generalized interpolation material point method, Comput. Model. Eng. Sci. 5 (2004) 477–495.

[70] M. Steffen, P.C. Wallstedt, J.E. Guilkey, R.M. Kirbyand, M. Berzins, Examination and analysis of implementation choices within the material point method (MPM), Comput. Model. Eng. Sci. 31 (2) (2008) 107–127.

[71] A. Sadeghirad, R. Brannon, J. Burghardt, A convected particle domain interpolation technique to extend applicability of the material point method for problems involving massive deformations, Int. J. Numer. Methods Eng. 86 (2011) 1435–1456.

[72] Q.A. Tran, W.T. Sołowski, M. Berzins, J. Guilkey, A convected particle least square interpolation material point method, Int. J. Numer. Methods Eng. (2019) https://doi.org/10.1002/nme.6257.

[73] M. Steffen, R.M. Kirby, M. Berzins, Analysis and reduction of quadrature errors in the material point method (MPM), Int. J. Numer. Methods Eng. 76 (2008) 922–948.

[74] D. Sulsky, M. Gong, Improving the material point method, innovative numerical approaches for multi-field and multi-scale problems, Lect. Notes Appl. Comput. Mech. 81 (2016) 217–240.

[75] P.C. Wallstedt, J.E. Guilkey, Improved velocity projection for the material point method, Comput. Model. Eng. Sci. 19 (3) (2007) 223–232.

[76] J.U. Brackbill, The ringing instability in particle-in-cell calculations of low-speed flow, J. Comput. Phys. 75 (1988) 469–492.

[77] C. Gritton, M. Berzins, R. Kirby, Improving accuracy in particle methods using null spaces and filters, in: E. Onate, M. Bischoff, D.R.J. Owen, P. Wriggers, T. Zohdi (Eds.), Proceedings of the IV International Conference on Particle-Based Methods, Barcelona, Spain, 2015.

[78] C. Gritton, M. Berzins, Improving accuracy in the MPM method using a null space filter, Comput. Part. Mech. 3 (12) (2016) 1–12.

[79] Q.A. Tran, W.T. Sołowski, Temporal and null-space filter for the material point method, Int. J. Numer. Methods Eng. 120 (3) (2019) 328–360.

[80] R. Courant, K. Friedrichs, H. Levy, On the partial difference equations of mathematical physics, IBM J. Res. Dev. 11 (2) (1967) 215–234.

[81] R. Brannon, https://csmbrannon.net/2016/01/04/the-kinematic-anomaly-in-mpm/ [online], 2016.

[82] C. Jiang, C. Schroeder, J. Teran, An angular momentum conserving affine-particle-in-cell method, J. Comput. Phys. 338 (2017) 137–164.

[83] M. Berzins, Nonlinear stability and time step selection for the MPM method, Comput. Part. Mech. 5 (2018) 455–466.

[84] I. Vardoulakis, Scherfugenbildung in Sandkörpern als Verzweigungsproblem, Dissertation 70, Institute for Soil and Rock Mechanics, University of Karlsruhe, 1977.

[85] I. Vardoulakis, M. Goldscheider, In: Biaxial Apparatus for Testing Shear Bands in Soils, Proc. 10th Conf. Soil Mech. Found. Engng., Stockholm, 1981, pp. 819–824.

[86] J. Tejchman, I. Herle, J. Wehr, FE-studies on the influence of initial density, pressure level and mean grain diameter on shear localisation, Int. J. Numer. Anal. Methods Geomech. 23 (15) (1999) 2045–2074.

[87] J. Tejchman, Numerical simulations of filling in silos with a polar hypoplastic constitutive model, Powder Technol. 96 (3) (1998) 227–239.

[88] C. González-Montellano, A. Ramírez, J.M. Fuentes, F. Ayuga, Numerical effects derived from 'en masse' filling of agricultural silos in DEM simulations, Comput. Electron. Agric. 81 (2012) 113–123.

[89] Eurocode 1, BS EN 1991–4: Actions on Structures. Part 4: Silos and Tanks. General Principles and Actions for the Structural Design of Tanks and Silos, 2006.

[90] M. Guaita, A. Couto, F. Ayuga, Numerical simulation of wall pressure during discharge of granular material from cylindrical silos with eccentric hoppers, Biosyst. Eng. 85 (1) (2003) 101–109.

[91] J. Tejchman, J. Górski, FE study of patterns of shear zones in granular bodies during plane strain compression, Acta Geotech. 5 (2) (2010) 95–112.

[92] J. Tejchman, J. Górski, Modeling of bearing capacity of footings on sand within stochastic micro-polar hypoplasticity, Int. J. Numer. Anal. Methods Geomech. 35 (2) (2011) 226–243.